Addressing complexities in MPM modeling of calibration chamber cone penetrometer tests in homogenous and highly interlayered soils

Yost, Kaleigh M.; Martinelli, Mario; Yerro, Alba; Green, Russell A.; de Lange, Dirk A.

DOI
10.1016/j.compgeo.2023.105378

Publication date
2023

Document Version
Final published version

Published in
Computers and Geotechnics

Citation (APA)
Yost, K. M., Martinelli, M., Yerro, A., Green, R. A., & de Lange, D. A. (2023). Addressing complexities in MPM modeling of calibration chamber cone penetrometer tests in homogenous and highly interlayered soils. *Computers and Geotechnics*, *158*, Article 105378. https://doi.org/10.1016/j.compgeo.2023.105378

Computers and Geotechnics 158 (2023) 105378

Contents lists available at ScienceDirect

Computers and Geotechnics

journal homepage: www.elsevier.com/locate/compgeo

Addressing complexities in MPM modeling of calibration chamber cone penetrometer tests in homogenous and highly interlayered soils

Kaleigh M. Yost [a,*], Mario Martinelli [b,c], Alba Yerro [a], Russell A. Green [a], Dirk A. de Lange [b]

[a] Dept. of Civil and & Environmental Engineering, Virginia Tech, Blacksburg, VA, USA
[b] Geo-Engineering Unit, Deltares, Delft, Netherlands
[c] Faculty Civil Engineering & Geosciences, Technical University of Delft, Netherlands

ARTICLE INFO

Keywords:
MPM
CPT
Calibration chamber
Interlayered soils

ABSTRACT

Cone penetrometer tests (CPTs) are used to characterize soil for a variety of geotechnical engineering applications, including earthquake-induced liquefaction triggering assessment. Numerical modeling of CPTs is frequently used to better understand soil behavior, soil-penetrometer interaction, and engineering estimates made from CPT data. However, calibrating and validating numerical CPT simulations with experimental calibration chamber (CC) data can be challenging. Specifically, uncertainties in the interpretation of laboratory strength and compression data compound with uncertainties in the CC testing and the assumptions made when developing the numerical model. This article provides a comprehensive review of uncertainties in the calibration and validation of CPT numerical simulations performed in homogenous sand, homogenous clay, and layered sand-clay soil profiles, comparing numerical results with well-documented experimental calibration chamber tests performed at Deltares. In particular, the Material Point Method (MPM) is used to perform the numerical analyses. A framework is presented to assess how uncertainty in the numerical model output is attributed to each input parameter. It is demonstrated that uncertainties can be explored numerically. Finally, recommendations for future experimental and numerical studies of CPTs are provided.

1. Introduction

Cone penetrometer tests (CPTs) are a popular in-situ method to characterize soil profiles for geotechnical engineering applications like earthquake-induced liquefaction triggering assessment. Numerical simulations of CPTs are useful for understanding soil behavior, soil-penetrometer interaction, and estimating engineering parameters made using CPT data. These simulations are typically calibrated and validated using laboratory calibration chamber (CC) data. While much work has been done experimentally and numerically to study CPTs in homogenous soil profiles, very little has been done to understand CPTs in highly interlayered soil profiles. To date, two experimental CC studies on highly interlayered profiles have been conducted in the lab, the one explored herein by De Lange (2018), and a recent one by Skrede et al. (2022). Direct numerical simulations of CPTs in interlayered soil profiles have also only recently been studied by Yost et al. (2022).

Experimental tests and numerical simulations of CPTs in interlayered soil profiles are often used to study multiple thin-layer effects, a phenomenon in which CPT data are blurred or averaged in interlayered soils, resulting in inaccurate engineering calculations made using those data (e.g., Boulanger and DeJong, 2018; Yost et al., 2021; Cooper et al., 2022). The presence of multiple soil types in the experimental and numerical analyses of CPTs introduces significantly more complexity and motivated the investigations presented in this paper. Understanding the limitations of experimental and numerical CPT models in both homogenous and layered profiles is critical to the development of more effective correction procedures for multiple thin-layer effects. The behavior of a CPT in a layered sand-clay profile, for example, is directly linked to the hypothetical behavior of the CPT in homogenous sand and homogenous clay profiles under the same conditions as the layered profile. Therefore, both homogenous and layered profiles are examined in this study.

Herein, we explore the nuances of calibrating numerical models with experimental CC CPTs by back-analyzing the CC tests performed by De Lange (2018). This study is unique because numerical modelers typically rely on experimental results from external studies to calibrate their models, whereas the work discussed in this article was a collaboration between the numerical and experimental modelers. Experimental factors that negatively impacted the ability to calibrate the numerical

* Corresponding author.
E-mail address: kmyost@vt.edu (K.M. Yost).

https://doi.org/10.1016/j.compgeo.2023.105378
Received 17 November 2022; Received in revised form 1 March 2023; Accepted 2 March 2023
Available online 20 March 2023

Nomenclature

Notation

a	adhesion between cone and clay
b	exponent of the stiffness relation
C_u	coefficient of uniformity
d_{cone}	diameter of the cone
D_R	relative density
d_{50}	mass-median-diameter
E	Young's modulus
e	void ratio
e_0	initial void ratio
e_{cs}	critical state void ratio
$e_{cs,o}$	critical state void ratio at p'=0
e_{max}	maximum void ratio
e_{min}	minimum void ratio
e^*_{min}	void ratio at which volumetric strains are negligible (elasticity parameter)
G	shear modulus
G_{ref}	shear modulus factor
H	hardening modulus
I_R	rigidity index
K_0	coefficient of at-rest lateral earth pressure
LL	liquid limit
m	exponent of critical state line
N	dilatancy parameter
n	porosity
n_o	initial porosity
n_{max}	maximum porosity
n_{min}	minimum porosity
p_a	atmospheric pressure
p'	mean effective stress
PL	plastic limit
q	deviatoric stress
q_c	tip resistance
$\bar{q}_c$	average tip resistance
s_u	undrained shear strength
w	water content
ε_a	axial strain
λ	slope of the critical state line
ν	Poisson's ratio
ρ_{grains}	density of particles
φ_{cont}	contact friction angle between cone and sand
φ_{cs}	critical state friction angle
σ'_h	horizontal effective stress
σ'_{ho}	initial horizontal effective stress
σ'_v	vertical effective stress
σ'_{vo}	initial vertical effective stress
χ	dilatancy coefficient
ψ	state parameter
ψ_o	initial state parameter

model are discussed at length, as well as the shortcomings and limitations of the numerical model – both items which are typically glossed over in literature. We highlight the role of uncertainty in calibration procedures and propose methods to reduce uncertainty in future experimental and numerical CC studies. The results of this study will help inform best-practices of future experimental and numerical studies of CPTs in both homogenous and layered soil profiles, as well as help provide better data to develop multiple thin-layer correction procedures for CPTs in highly interlayered soil profiles.

The objectives of this work are to: (1) demonstrate the complexity of calibrating MPM CPT simulations with CC studies; (2) quantify how uncertainty in the MPM model's output (tip resistance, q_c) is attributed to various input parameters; and (3) demonstrate how uncertainty can be accounted for in the MPM simulations. In Section 2, we review previous experimental CC tests and MPM simulations of CC tests. The experimental CC tests and MPM model used in this study are detailed in Section 3 and Section 4, respectively. In Section 5, we present a framework to quantify uncertainty in the MPM model input and output. We demonstrate how uncertainty can be addressed in the MPM simulations and discuss how to reduce uncertainty in both experimental and numerical CC tests in Section 6. The contents of the article are summarized in Section 7.

2. Background

2.1. Calibration chamber tests

The experimental CCs discussed in this paper consist of large (~1 m in height and diameter, or larger), cylindrical vessels into which a soil specimen is prepared, confining stresses are applied, and various types of penetration testing are performed. The first large CCs were developed in the late 1960s and early 1970s and were used to study penetration in dry sands to improve settlement predictions (Chapman, 1974; Holden, 1991). Over the next ~20 years, several more CCs were constructed, and more complex tests were performed. Furthermore, owing to the expensive and time-consuming nature of CC testing, many researchers began to supplement experimental CC tests with numerical simulations of CC tests. Approximately 40 years of research culminated in the 1st International Symposium on Calibration Chamber Testing in 1991. The proceedings (Huang, 1991) highlighted three key attributes of CC tests that are influential to the results of penetration testing (i.e., q_c) and relevant to the discussion in this study: (1) CC radius, (2) CC boundary conditions, and (3) soil type and profile preparation; each is discussed in further detail subsequently.

1. Much attention has been given to size effects or how the ratio of the CC diameter to penetrometer diameter, d_{cone}, impacts q_c. Since the radial extent of a CC does not replicate free-field conditions, one expects a difference in q_c obtained in the lab compared to the field. Generally, the larger the CC-to-cone-diameter ratio, the less impactful the size effects are (e.g., Mayne and Kulhawy, 1991). Furthermore, size effects are generally less apparent (and sometimes not apparent at all) in CPTs performed in looser sands compared to denser sands (e.g., Parkin and Lunne, 1982; Ghionna and Jamiolkowski, 1991; Schnaid and Houlsby, 1991; Fioravante et al., 1991). Salgado et al. (1998) elaborated on this observation, stating that heavily dilatant sands will be more impacted by size effects than compressive sands.
2. The type of CC boundary conditions impact q_c and can make size effects more or less apparent. Typically, either a constant pressure (flexible) or a zero strain (rigid) radial boundary condition is used in CC testing (some of the most common conditions are described by Salgado et al. 1998). Generally, flexible lateral boundary conditions result in lab q_c values lower than what they would be in the free-field (e.g., Mayne and Kulhawy, 1991). Fioravante et al. (1991) showed that CPTs in very dense Toyoura sand prepared in a CC with a CC-to-cone-diameter ratio of ~ 34 produced a smaller q_c under flexible radial boundary conditions than rigid conditions, noting that increased horizontal stresses during penetration in the latter case resulted in an elevated q_c. Although Salgado et al. (1998) predicted that rigid radial boundary conditions will produce q_c values that poorly represent free-field conditions, there is some evidence

otherwise. Huang et al. (1991) performed numerical simulations of CC tests and observed that CPTs performed with a rigid radial boundary produced q_c closer to the field condition than CPTs performed with a flexible boundary. Similarly, Butlanska et al. (2010)'s CPT simulations in very dense sand under ~ 50 kPa horizontal confining stresses showed that size effects are observed using a flexible radial boundary but are not observed when using a rigid boundary. A study by Pournaghiazar et al. (2013) showed using spherical cavity expansion theory that a CC-to-cone-diameter ratio of at least 35 is required to avoid boundary effects for either rigid or flexible radial boundaries, but if cylindrical cavity expansion theory is used, a ratio of at least 140 (i.e., a chamber with ~ 5 m diameter for a standard ~ 36 mm diameter cone) is required to avoid boundary effects for a flexible radial boundary. An even greater ratio is required for a rigid radial boundary. Spherical cavity expansion theory is commonly used to model cone penetration, but Salgado and Prezzi (2007) argue that cylindrical cavity expansion is more appropriate. With this in mind, existing experimental calibration chambers are unlikely to ever meet the diameter requirements to avoid boundary conditions altogether, regardless of boundary condition.

3. The q_c measured in a CC test is influenced by soil type and sample preparation; thus, controlled and repeatable preparation techniques are required to achieve uniformity throughout the sample (e.g., Eid, 1987; Ghionna and Jamiolkowski, 1991). Different soil types or sample preparation may result in varied impacts on q_c from size effects and boundary conditions.

In summary, q_c obtained from experimental CC tests is dependent on test-specific and soil-specific conditions, which are often intertwined. This makes it difficult to extrapolate expected trends from literature to unique modeling/testing scenarios. Of particular interest to this study is CPT behavior in interlayered soils, which adds additional complexities. There is very little literature on experimental CC tests performed on interlayered soil profiles, with tests performed by De Lange (2018) and, more recently, by Skrede et al. (2022) being the only ones known to the authors. Further exploration of how CPTs perform in interlayered soil profiles in experimental and numerical CCs with different conditions is therefore warranted.

2.2. MPM models of CPTs

Numerical modeling of CPTs must be able to account for large soil deformations and complex contact interactions between the penetrometer and the soil. In this study, MPM is utilized. MPM is a combined mesh- and particle-based numerical method that operates within a continuum framework. MPM was first developed by Sulsky et al. (1994) and has since been used for a variety of different applications involving large deformations. Many researchers have successfully used MPM to simulate cone penetration in clays and sands with increasingly complex conditions. Beuth and Vermeer (2013) simulated CPTs in undrained clay using implicit MPM. This work was extended for two-phase clay materials under varied drainage conditions with explicit MPM by Ceccato et al. (2015, 2016a, 2016b) and Ceccato and Simonini (2017). Since then, Bisht et al. (2021a, 2021b) have simulated CPTs in clay using a two-phase formulation of MPM that incorporates the generalized interpolation material point method (GIMP: Bardenhagen and Kober, 2004) to mitigate stress oscillations and a non-linear B-bar method (Simo et al., 1985) to reduce volumetric locking. The B-Bar method evaluates the strains and internal forces using a modified B-matrix (array containing the derivatives of the shape function) in which the isotropic components are evaluated at the center of the element.

MPM simulations of CPTs in sand have received similar attention. Al-Kafaji (2013) modeled pile installation in dry sand utilizing several concepts that have since been applied to cone penetration problems, like the moving mesh technique. Tehrani and Galavi (2018) performed CPT simulations in dry sand, and Galavi et al. (2018) introduced an axisymmetric formulation that significantly reduced computational costs. Ghasemi et al. (2018) studied CPTs in saturated, one-phase, drained sand using Mohr-Coulomb constitutive relationships. Martinelli and Galavi (2021) used a stress-dependent double-hardening constitutive model to simulate calibration chamber tests in dry, dense sand. Martinelli and Pisano (2022) showed that incorporating state-dependent constitutive models like NorSand (Jefferies, 1993) that model sand behavior over the wide range of stresses experienced during a CPT is possible and desirable. Recently, Martinelli and Galavi (2022) developed a coupled MPM formulation that uses quadrilateral elements and the B-bar method (Hughes, 2000) to reduce volumetric locking; this implementation is used in the present study.

These advancements in the numerical algorithms and constitutive capabilities of MPM make it possible to model CPTs accurately. However, they also require more input parameters and assumptions with their associated uncertainties. Furthermore, despite extensive research using MPM to study CPTs in homogenous soil profiles, Yost et al. (2022) is the only study known to the authors that showed the feasibility of using MPM to simulate CPTs in interlayered soil profiles. The presence of multiple soil types in these numerical models increases complexity and warrants further investigation.

3. Calibration chamber tests

A series of experimental CC tests performed at Deltares and detailed extensively by De Lange (2018) were used to calibrate and validate the numerical framework presented in Section 4. The following paragraphs provide pertinent information regarding the CC tests and quantify the uncertainties in the experimental setup, experimental methods, soil profile preparation, and soil properties that guide the development of the numerical model. The experimental uncertainties are mapped to numerical inputs, each of which is assigned a lower bound, upper bound, and baseline value. These values are used later in Section 5 to quantify how the uncertainty in the numerical model's output (q_c) is attributed to its various input parameters. Fig. 1 shows the identified experimental uncertainties (on the left) and the numerical parameters that are used to represent them (on the right). For example, the asymmetry of the CPT locations in the experimental methods is represented by varying the calibration chamber radius in the numerical model.

3.1. Experimental setup

The CC geometry is shown in Fig. 2a and b. The CC comprised a set of stacked cylindrical steel rings, 0.9 m in inner diameter. A hydraulic jacking unit and reaction frame was used to push a 25.3-mm-diameter penetrometer at 4 mm/sec to a maximum penetration of 0.75 m. The CC-to-cone-diameter ratio was ~35.7. This diameter was thought to be adequate to avoid boundary influences (e.g., per observations from references such as Pournaghiazar et al. 2013) since the intended radial chamber boundary condition was flexible. The sides of the chamber were lined with a flexible rubber membrane (~3 mm thick) and a porous geotextile (~2 mm thick) through which water was filled, intending to apply a constant radial pressure and eliminate friction along the wall (i.e., flexible boundary condition). However, due to the thinness and flexibility of the membrane and geotextile, and to the movement of the soil during cone penetration, we suspect that the gap between the rigid CC wall and the soil closed, making the radial boundary a rigid one. In the numerical sensitivity study presented herein, we consider both rigid and flexible radial boundaries to see their impact on the results, with the rigid boundary used as the baseline condition. It will be shown that the CC-to-cone-diameter ratio is not adequate to avoid boundary effects considering this fixed radial boundary condition, which is unsurprising considering the findings of Pournaghiazar et al. (2013), discussed in Section 2.2.

Saturated soil profiles 0.96 m in height were prepared within the

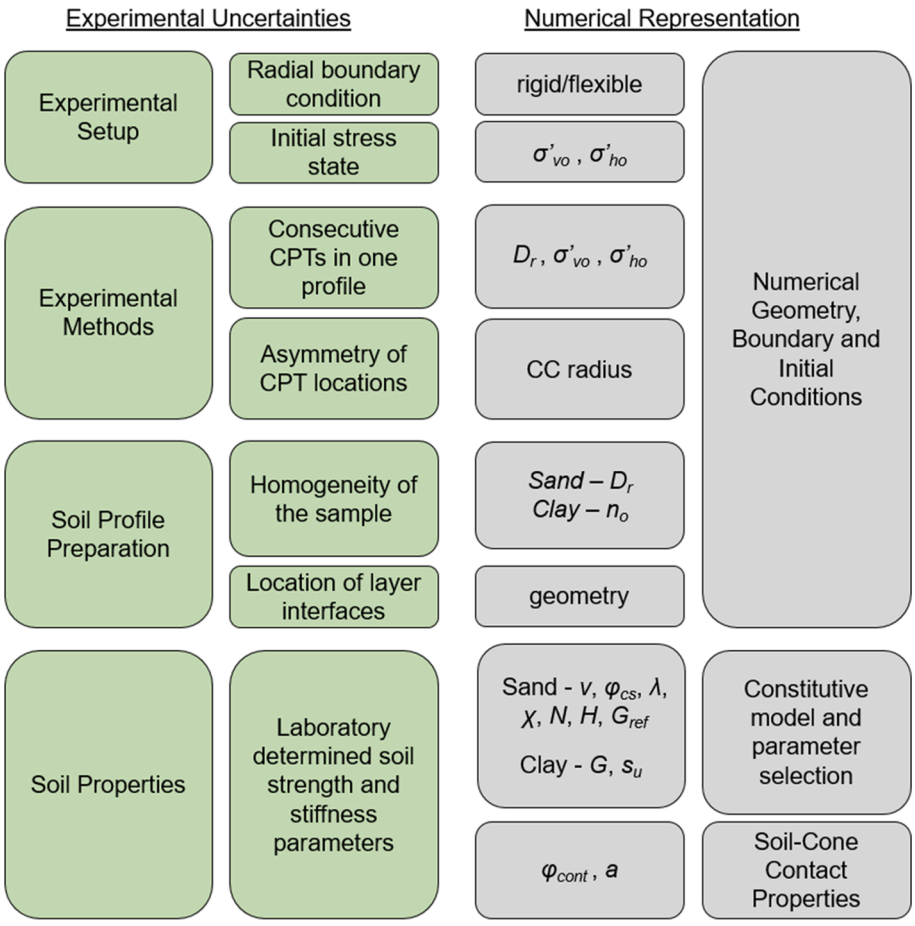

Fig. 1. Mapping experimental uncertainties to numerical parameters (see *Notation* for parameter definitions).

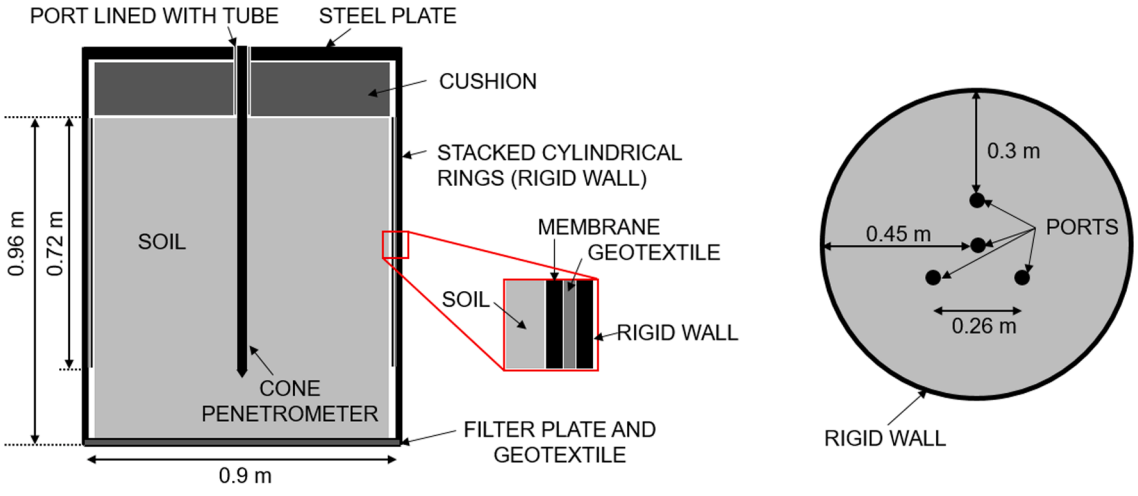

Fig. 2. Calibration chamber setup: (a) profile view, and (b) cross-sectional view.

annular space of the CC. Drainage was allowed through the rigid bottom of the CC via a geotextile and filter plate. A fluid-filled cushion at the top of the chamber applied vertical pressure to the soil. The cushion had several ports that allowed for drainage of the soil and for a penetrometer to be advanced through it. Typically, a set of three CPTs were performed in each soil profile that was constructed, and the initial vertical effective stress (σ'_{vo}) was increased prior to each subsequent CPT. The horizontal effective stress (σ'_{ho}) was initialized as $0.5\sigma'_{vo}$. However, there is some uncertainty in the reported initial stresses. For example, the cushion applying pressure to the top of the soil profile was made of foam covered by a relatively thick layer of silicon. The pressure measured in the cushion is not necessarily equal to the pressure acting on the top of the soil profile. To address the possible variation from the reported initial stress conditions, we varied σ'_{ho} by $\pm$ 10 kPa in the sensitivity analyses,

with the reported stress as the baseline condition.

3.2. Experimental methods

In the De Lange (2018) experiments, three CPTs were typically performed per soil profile in a triangular pattern, 0.26 m from each other and 0.3 m from the closest edge of the CC; see Fig. 2b. Ideally, this would be modeled numerically as a 3D problem, but this is prohibitively computationally expensive. We expect the 2D axisymmetric geometry used in this study to reasonably model the conditions, although, the numerical geometry is more difficult to define. Using the true 0.45-m radius of the chamber would not account for the presence of a rigid boundary that, at its closest, would be 0.3 m away from the CPT. Using a 0.3-m radius would underestimate the amount of soil being confined in the CC by about 44%. We decided to consider numerical models with both 0.3-m and 0.45-m radii, with the 0.45-m radius selected as the baseline condition.

The practice of performing more than one CPT per profile also appears to impact results. Based on one set of three tests performed in the same homogenous sand profile at the same applied σ'_{vo}, average tip resistance ($\bar{q}_c$) computed between 0.1 and 0.7 m tended to increase with each consecutive test, as shown in Fig. 3a. We will show that the impact of performing multiple CPTs in one soil profile can be accounted for numerically in Section 6.2.

3.3. Soil profile preparation

Both homogenous sand and layered sand-clay profiles were included in the De Lange (2018) study. Clay layers were constructed by placing bricks of trimmed, prefabricated clay side by side on top of a previously placed sand layer. Sand layers were created by pluviating dry sand from a constant height into the CC which was partially filled with water. An as-prepared relative density (D_R) was reported, but it is representative of the entire sand volume on average and does not capture local variations in density. Spatial variability in D_R was estimated as $D_R \pm 10\%$ by De Lange (2018) and is reflected in variations in q_c of up to ~20% from $\bar{q}_c$ in the experimental results; see Fig. 3 a,b. The uncertainty in as-prepared D_R is even greater for the layered soil profiles because of increased measurement uncertainty in the height of thinner layers. Furthermore, post-test local density measurements indicated increases in density, up to about $D_R + 20\%$. In the numerical simulations, we considered the reported as-prepared D_R as the baseline case and established upper and lower bounds as the baseline $D_R \pm 10\%$.

Another uncertainty in profile preparation is defining the exact depths of the embedded layer interfaces in the layered sand-clay profiles. For example, for the layered profile considered herein, experimental measurements taken at the time of profile preparation and after profile excavation indicate ~0.7 cm of total settlement in the profile over the course of testing. While depth to layer boundaries may be estimated using settlement theories, accuracy on the order of millimeters would be required to precisely pinpoint layer locations at the time each CPT was performed. Furthermore, there is uncertainty in how the depth readings are "zeroed" because the reference depth (depth at which the CPT enters the soil) may have been affected by the tubes used to protect the cushion from the penetrometer. The potential offset in depth from these factors is small (on the order of millimeters). However, it is enough to potentially explain observed differences in the location of peaks and troughs in q_c when comparing numerical and experimental data, which have previously been thought to be related to limitations in the definition of soil-cone contact properties in the numerical model (i.e., Yost et al. 2022). We did not address this issue in this study, but we acknowledge that small differences in the depths of the peaks and troughs of q_c in the experimental and numerical data can likely be attributed, at least in part, to uncertainty in the actual depths of the layer interfaces.

3.4. Soil properties

The soils used in the experiments were Baskarp B15 sand and Vingerling K147 clay. The sand is uniform and fine. Index properties were determined by De Lange (2018) and are shown in Table 1, but no strength tests were performed. The clay is an artificial lean clay produced by Sibelco. De Lange (2018) performed index testing (see Table 1), one constant rate of strain consolidation test, and a series of

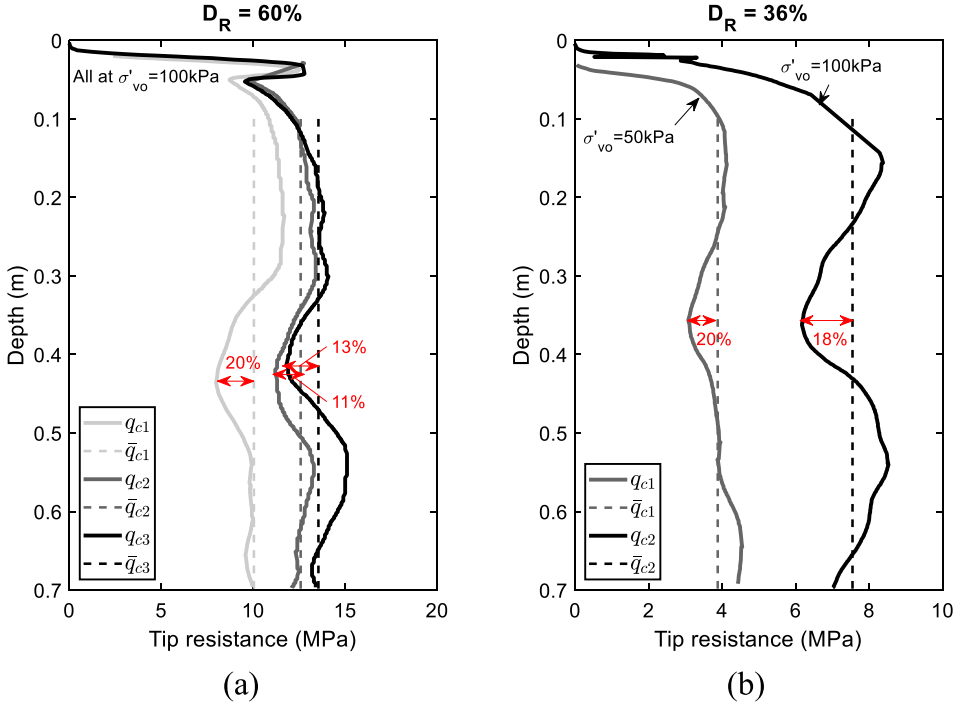

Fig. 3. Variability in experimental tip resistance (q_c) for CPTs performed in homogenous sand profiles during the De Lange (2018) study: (a) Three CPTs performed at $\sigma'_{vo} = 100$ kPa with $D_R = 60\%$, and (b) One CPT performed at $\sigma'_{vo} = 50$ kPa and one at $\sigma'_{vo} = 100$ kPa with $D_R = 36\%$.

Table 1
Index properties soil used in CC tests.

Soil	Parameter	Symbol (Unit)	Value
Sand	Mass-median-diameter	d_{50} (mm)	0.136
	Coefficient of uniformity	C_u (-)	1.4
	Density of particles	ρ_{grains} (kg/m^3)	2650
	Minimum porosity	n_{min} (%)	35.6
	Maximum porosity	n_{max} (%)	47.1
	Minimum void ratio	e_{min} (-)	0.552
	Maximum void ratio	e_{max} (-)	0.890
Clay	Water content	w (%)	22.8
	Liquid Limit	LL (%)	32.3
	Plastic Limit	PL (%)	15.8

four anisotropically consolidated, undrained (ACU) triaxial tests on the clay. Because the clay was extruded in a vacuum press, it has a pre-consolidation pressure of approximately 80 kPa based on the consolidation and ACU test results. After preparing the soil profile in the CC and applying an overburden stress, the clay layers were allowed to consolidate to 90%. In the MPM simulations, the uncertainties associated with the soil properties were addressed through a sensitivity analysis of the constitutive model parameters selected to represent soil behavior. Extensive details regarding the selection and calibration of the constitutive models are provided in Sections 4.2 and 4.3.

4. Numerical model

A 2D axisymmetric MPM model was created to replicate several CC tests described in Section 3. The following sections detail the implementation, geometry, mesh, boundary conditions, and constitutive modeling used in these analyses.

4.1. Model implementation, geometry, mesh, and boundary conditions

The explicit MPM implementation utilized for this study is detailed extensively in Martinelli and Galavi (2022), and thus, is only briefly summarized herein. The implementation uses linear, 4-noded quadrilateral elements and a Gauss integration scheme to mitigate stress oscillations. To minimize volumetric locking, the B-bar method (Hughes, 2000) is implemented, in which only the integration point at the center of an element is used to compute volumetric strains. A mass scaling factor of 10,000 was used to expedite the calculations. A Courant number of 0.95 was used.

The geometry and mesh are shown in Fig. 4. The height of the model was 2 m, and the bottom 1 m of the domain represented the soil profile. The radial dimension extended either to 0.3 or 0.45 m, depending on the simulation (see Section 3.2). The density of the surcharge layer (blue layer in Fig. 4) was adjusted to get $\sigma'_{vo} = 50$ kPa at the top of the soil to match CC conditions. Contact between the surcharge layer and penetrometer was assumed to be perfectly smooth. Stresses were initialized using an at-rest lateral earth pressure (K_0) procedure with $K_0 = 0.5$. The left boundary was fixed in the x-direction, and the bottom boundary was fixed in the y-direction. The right (radial) boundary was either fixed in the x-direction to represent a rigid boundary (baseline condition) or represented as a thin layer of very soft ($E = 1$ kPa) linear elastic soil that maintained a nearly constant radial stress to represent a flexible boundary (the same technique used by Martinelli and Pisano, 2022).

The 25.3-mm-diameter penetrometer with a 60-degree apex angle was "wished into place" at the left boundary (i.e., the axis of symmetry) and embedded 21.91 mm (the height of the conical face) into the soil profile. The cone was modeled as rigid and was advanced at a constant velocity of 40 mm/sec (the experimental CC experiments advanced the cone at 4 mm/sec; however, because the solution is independent of the penetration velocity, a larger value was used for computational speed). The domain was discretized using a moving mesh (Beuth, 2012) and compressing mesh to maintain the shape of the soil-cone contact elements throughout the simulation. The compressing mesh was structured with element widths of about $0.25d_{cone}$ within the penetration zone. The moving mesh was unstructured and finely discretized (widths of $\sim 0.25d_{cone}$ or less) around the tip of the penetrometer. The discretization was coarser with increasing distance from the penetrometer. Similarly, material points (MPs) in the soil were assigned in a grid comprising four

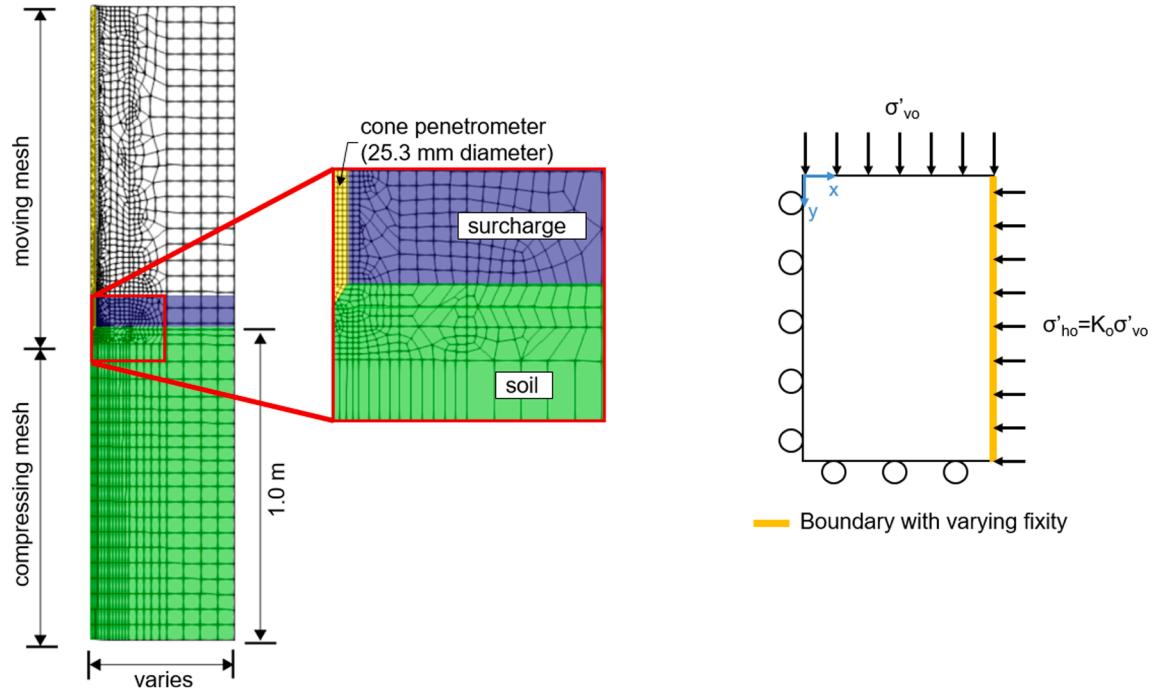

Fig. 4. (a) Geometry and mesh of 2D axisymmetric model, and (b) boundary conditions.

zones, with MP density decreasing with increasing radial distance from the penetrometer. The first zone was ~0.06 m wide and contained 70 columns and 650 rows of MPs, the second was ~0.06 m wide and contained 25 columns and 400 rows of MPs, the third was ~0.12 m wide and contained 35 columns and 300 rows of MPs, and the fourth was ~0.31 m wide and contained 20 columns and 250 rows of MPs. Each element in the penetrometer was assigned one MP.

4.2. Constitutive modeling of sand

The constitutive behavior of the saturated Baskarp B15 sand was modeled with the Jefferies and Been (2015) description of NorSand implemented by Martinelli (2019). Since no strength or stiffness testing was performed on the sand as a part of the De Lange (2018) study, consolidated drained (CD) triaxial test data collected by Ibsen and Bødker (1994) on the same sand were used to determine the NorSand model parameters (see Table 2). The following paragraphs contain an overview of how these parameters were selected. Complete details are provided in the supplemental materials to this article.

An exponential critical state line (CSL) formulation proposed by Li and Wang (1998) was adopted instead of the log-linear one used by Jefferies and Been (2015). The exponential form has been shown to better capture soil behavior at large mean effective stresses (p') expected during cone penetration (Martinelli and Pisano, 2022) and is defined by:

$$e_{cs} = e_{cs,o} - \lambda\left(\frac{p'}{p_a}\right)^m \tag{1}$$

where e_{cs} is the critical state void ratio, p_a is atmospheric pressure in the same units as p', and $e_{cs,o}$, λ, and m are the CSL parameters defined in Table 2. The CSL parameters were determined using CD triaxial tests performed on specimens in very loose states ($D_R = 1\%$) and tested over a wide range of confining stresses. The e-p' behavior associated with each test is plotted in Fig. 5. Instead of drawing a single CSL for this set of tests, a plausible zone where the CSL may fall is defined. To make it easier to assess the uncertainty in CSL location without having to change multiple parameters, two CSL parameters are held constant (namely, $e_{cs,o} = 0.90$ and $m = 0.7$), and the third (λ) is varied between 0.009 and 0.015 to define the boundaries of the plausible critical state zone (shaded zone in Fig. 5). Those λ values are used as the upper and lower bound parameters for the sensitivity analysis.

The elasticity relationship utilized in NorSand is defined as:

$$G = G_{ref}\frac{1}{e - e^*_{min}}p_a\left(\frac{p'}{p_a}\right)^b \tag{2}$$

where G is the shear modulus, G_{ref}, b, and e^*_{min} are elasticity parameters defined in Table 2, and all other variables are as previously defined. The elasticity parameters were determined based on results from bender element tests performed on Baskarp B15 sand by Bødker (1996). Similar

Table 2
Estimated Constitutive Parameters of Baskarp B15 Sand.

Parameter	Symbol	Baseline	Lower Bound	Upper Bound
Critical state void ratio at p'=0	$e_{cs,o}$	0.90	–	–
Slope of critical state line	λ	0.012	0.009	0.015
Exponent of critical state line	m	0.7	–	–
Shear modulus factor	G_{ref}	743	700	800
Exponent of the stiffness relation	b	0.57	–	–
Void ratio at which volumetric strains are negligible	e^*_{min}	0.051	–	–
Critical state friction angle	φ_{cs}	30	29	31
Dilatancy parameter	N	0.1	0.1	0.3
Dilatancy coefficient	χ	2.7	2.5	3.5
Poisson's ratio	ν	0.2	0.1	0.3
Hardening modulus	H	25	25	75

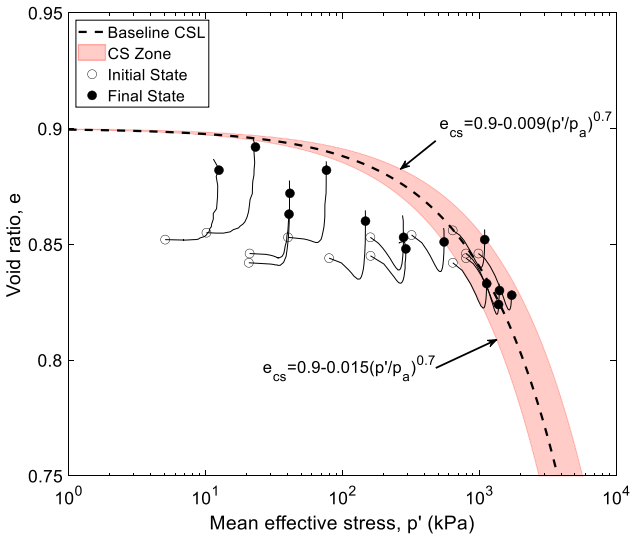

Fig. 5. Critical state line for Baskarp B15 sand based on 14 CD triaxial tests performed on loose specimens with $D_R = 1\%$. All triaxial data are from Ibsen and Bødker (1994).

to the approach taken to quantify uncertainty in the CSL, the only elasticity parameter that was modified in subsequent analyses was G_{ref}, between 700 and 800 (with $G_{ref} = 743$ as the baseline), as shown in Table 2. The parameters b and e^*_{min} were held constant.

The CD triaxial tests performed on dense ($D_R = 80\%$) and medium dense ($D_R = 51\%$) specimens were used to determine the dilatancy parameters N and χ, and critical state friction angle φ_{cs}, using the procedure described by Shuttle and Jefferies (2010). The baseline, upper, and lower bound values for these parameters are provided in Table 2. Note that because the baseline N and χ were already on the low end of the typical range for those parameters provided by Shuttle and Jefferies (2010), the lower bounds were selected to be equal to, or very close to, the baseline. The baseline value of Poisson's ratio, ν, was assumed to be 0.2, and the upper and lower bounds of ν were set based on typically assumed values.

The remaining parameter H is a NorSand model parameter that is calibrated by performing numerical single-element tests to replicate results from drained triaxial tests. H may be assumed constant throughout the simulation or described dynamically as a function of the current state parameter, ψ (Jefferies and Been, 2015). For this analysis, we assumed a constant H that was a function of the initial state parameter, ψ_o. To calibrate H, we aimed to match the initial stiffness of each considered laboratory triaxial test by varying H and holding all other parameters constant at baseline values provided in Table 2. In total, 12 of the CD triaxial tests were used for this calibration, and the results are shown in Fig. 6.

In general, we can match the experimental deviator stress-axial strain (q-ε_a) results relatively well for the dense, medium-dense, and loose data sets. The volumetric strain-axial strain (ε_v-ε_a) and void ratio-mean effective stress (e-p') results are a good match for the dense data (Fig. 6 a,b,c), and progressively less so for the medium-dense (Fig. 6 d,e, f) and loose (Fig. 6 g,h,i) data. We expect the match to be the worst for the loose data, which have initial states very close to the CSL – uncertainty in CSL location therefore has a larger impact on the results. A linear relationship between H and ψ_o was defined. However, results showed that H was also a function of initial mean effective stress (p'_o) as shown in Fig. 7. To reflect the considerable scatter in the data, a large range of possible H values was defined for the MPM analyses with a lower bound of 25 and an upper bound of 75, based on the ψ_o of the sand in the experimental CC tests that were being replicated. The lower bound value of 25 was also used as the baseline because it was observed to produce better matches between the numerical and experimental CPT

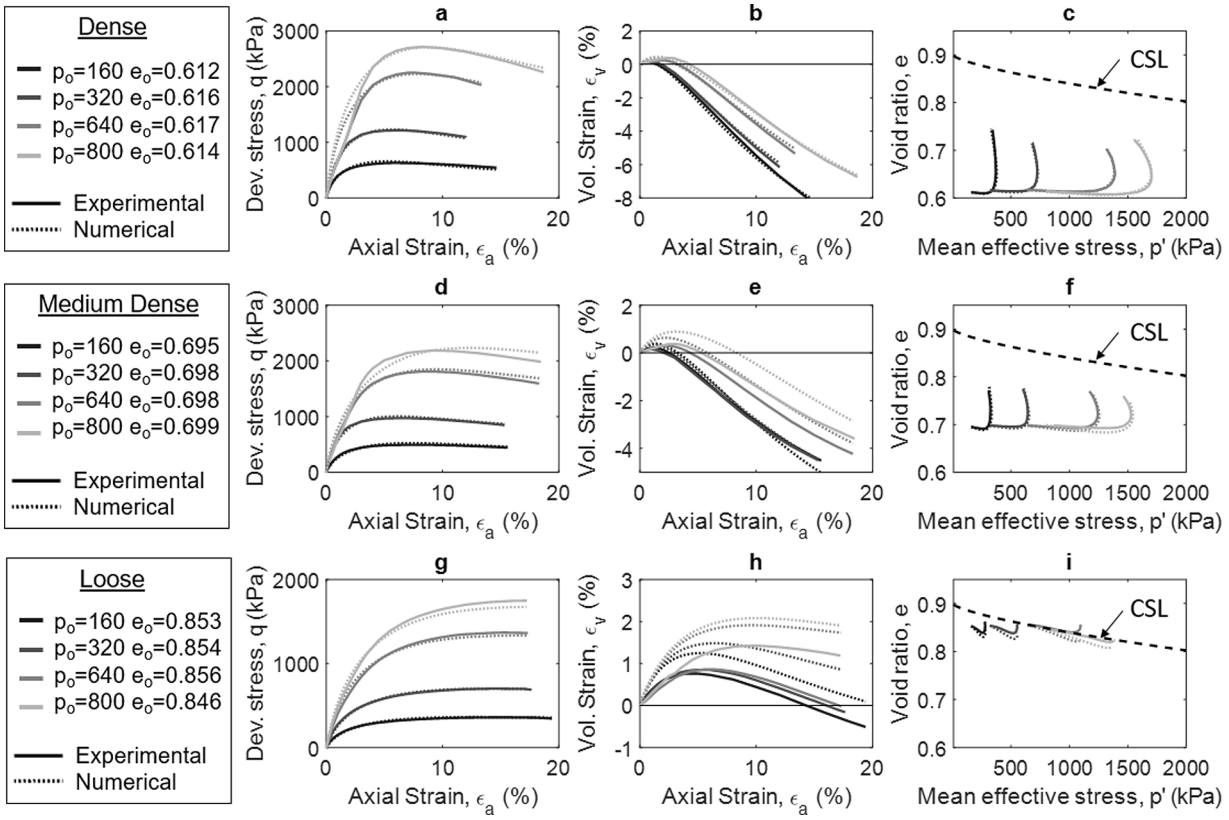

Fig. 6. Comparison of numerical and experimental triaxial data from Ibsen and Bødker (1994). (a-c) Dense specimens; (d-f) Medium dense speciments; (g-i) Loose specimens.

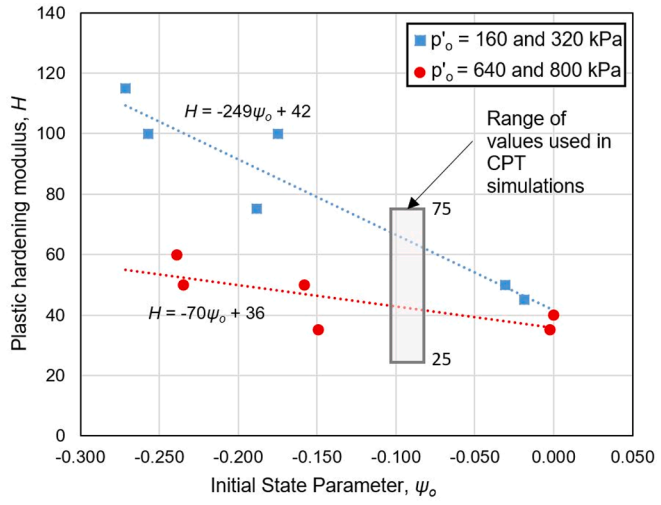

Fig. 7. Calibration of hardening modulus, *H*.

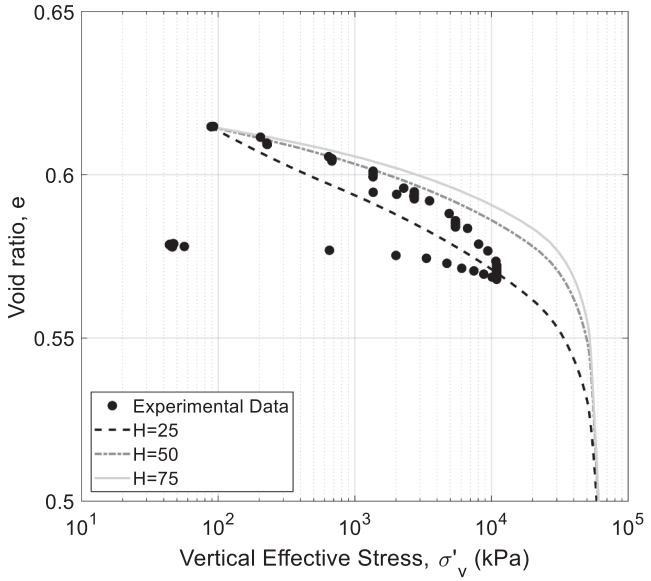

Fig. 8. Comparison of experimental and numerical oedometer results for various values of hardening modulus, *H*.

data.

Note that while the constitutive parameters of the NorSand model are calibrated using drained triaxial data, the complex stress path of the soil surrounding the cone during penetration is not anticipated to match that of a triaxial test. By exploring ranges of constitutive parameter inputs, instead of single values, a more realistic CPT response may be captured. To further address this limitation, the calibrated NorSand model was used to simulate an oedometer test conducted at similar stress levels to those experienced in the chamber. As shown in Fig. 8, the numerical model predicted the oedometer loading path reasonably well over the range of *H* values selected based on triaxial data, increasing the confidence in the results. However, it is important to note that all numerical models are limited in their ability to accurately simulate real soil behavior, due to uncertainty in the actual load paths and limited experimental data needed to further validate the models. Furthermore, microscale phenomena such as grain crushing (which was observed during constant load periods of the experimental oedometer test and may be occurring during cone penetration) is not explicitly captured by

the NorSand constitutive model.

4.3. Constitutive modeling of clay

The Tresca constitutive model was used to represent the saturated Vingerling K147 clay behavior. Tests conducted by De Lange (2018) were used to establish the baseline constitutive parameters summarized in Table 3.

The initial porosity (n_o) corresponds to the porosity after consolidation occurred in the CC. The undrained shear strength (s_u) and secant shear modulus at 50% of the mobilized strength (G) were determined based on results from an ACU triaxial test performed at a vertical effective consolidation stress ($\sigma'_{v,cons}$) equal to 50 kPa. Note that the rigidity index ($I_R = G/s_u$) corresponding to the baseline parameters is 20, considerably lower than the typical range of 50–500 (e.g., Krage et al., 2014). However, because Vingerling clay is an artificial clay and because the tests were performed under relatively low confining pressures, we think this I_R value is representative. The lower and upper bounds of G provide a range of I_R from 15 to 50. The value of the undrained Poisson's ratio was 0.4995.

4.4. Soil-cone contact

Contact between the soil and cone is modeled using the Bardenhagen et al. (2001) contact algorithm with the additions of Al-Kafaji (2013) for adhesive soils. If two different types of soil with different contact properties share the same contact node, then an average contribution is computed (e.g., Talmon et al., 2019). Soil-cone contact properties are typically assumed to be a fraction of the sand's φ or the clay's s_u. In these analyses, the sand-cone contact friction angle (φ_{cont}) was varied from $0.3\varphi_{cs}$ to $0.9\varphi_{cs}$ based on the range of typical aluminum-sand contact properties reported by Durgunoglu and Mitchell (1973), with the baseline set to $0.5\varphi_{cs}$. The contact adhesion (a) was varied from $0.25s_u$ to $0.5s_u$ based on the range of typical steel-clay contact properties reported by Potyondy (1961), with the baseline condition set to $0.5s_u$.

5. Sensitivity analysis

MPM simulations were performed for three soil profiles: one homogenous sand profile prepared at $D_R = 36\%$, one homogenous clay profile, and one layered sand-clay profile with 40-mm-thick layers and sand prepared at $D_R = 29\%$. Initial stress conditions for each simulation were the same with $\sigma'_{vo} = 50$ kPa and $\sigma'_{ho} = 25$ kPa. The homogenous sand and layered sand-clay profiles had experimental counterparts from De Lange (2018) to compare to. For each of the three soil profiles, one MPM simulation was performed using the baseline set of input parameters described in Tables 2 and 3, producing the baseline q_c realization (e.g., as shown in Fig. 9). The baseline simulations considered a rigid radial boundary and a 0.45 m radius, as discussed in Sections 3.1 and 3.2. Subsequent simulations were performed in which only one input parameter was changed to either its upper or lower bound value, producing additional q_c realizations to compare to the baseline. Note the experimental and numerical data shown in Fig. 9 match quite well; however, there is some discrepancy, especially at shallow depths. This can be attributed, at least in part, to boundary effects at the top of the chamber and compaction of the sand near the surface caused by placement of the heavy cushion, neither of which are accounted for by the numerical model. For the homogenous profile, a slight increase in q_c with depth is observed in the numerical results. This increase is due to the stress gradient within the soil profile in the chamber; a constant vertical stress is applied at the top boundary, but vertical stress increases with depth due to the weight of the soil.

Table 3
Estimated Constitutive Parameters of Vingerling K147 Clay.

Parameter	Symbol (Unit)	Baseline	Lower Bound	Upper Bound
Initial porosity	n_o (-)	0.362	0.290	0.434
Undrained shear strength at $\sigma'_{v,cons} = 50$ kPa	s_u (kPa)	27.9	22.3	33.5
Secant Shear Modulus	G (kPa)	552	423	1404

5.1. Quantifying changes in tip resistance

A representative $\bar{q}_c$ for each MPM realization was defined over a depth interval dependent on the soil profile type. For the homogenous sand and clay profiles, $\bar{q}_{c,sand}$ or $\bar{q}_{c,clay}$ was computed by averaging q_c values between 0.5054 and 0.5255 m (as shown in Fig. 9a for the homogenous sand baseline realization). For the layered profile, two $\bar{q}_c$ values were determined within the layered zone: $\bar{q}_{c,embsand}$ associated with the first embedded sand layer (q_c averaged over a 0.0023-m interval centered at the depth of the numerical peak at 0.3082 m) and $\bar{q}_{c,embclay}$ associated with the first embedded clay layer (q_c averaged over a 0.0042-m interval centered at the depth of the numerical trough at 0.2771 m). This is illustrated in Fig. 9b for the baseline realization in the layered profile. Note that defining $\bar{q}_{c,embsand}$ and $\bar{q}_{c,embclay}$ over small intervals for the embedded layers was necessary because q_c tended to reach a peak/trough value and then immediately start to decrease/increase, never reaching a fully developed value within a given embedded layer.

To compare results between realizations, a sensitivity index (SI) after Hoffman and Gardner (1983) was defined as:

$$SI = \left(q_{c,upperbound} - q_{c,lowerbound}\right) / q_{c,upperbound} \quad (3)$$

where $q_{c,upperbound}$ and $q_{c,lowerbound}$ are the $\bar{q}_c$ values computed from the realizations using the upper and lower bounds of a particular parameter.

Because the numerical simulations are dynamic, there is a level of noisiness, or variation from the mean in the numerical q_c, that can make interpreting results difficult. For example, changing one input parameter may produce a slight increase in $\bar{q}_c$; however, that increase may just be due to a slightly different combination of numerical noise. To keep the magnitude of SI in perspective, an SI associated with the noise level (SI_{noise}) in each baseline realization was computed over the same depth interval used to compute $\bar{q}_c$. For example, in Fig. 9b, $\bar{q}_{c,embsand}$ was computed over the depth interval 0.3071 to 0.3094 m. SI_{noise} for the embedded sand layer was computed as the difference between the maximum and minimum q_c values within that interval divided by the maximum q_c value, or (1637–1552)/1637 = 0.0519. Computed in the same way, SI_{noise} for the embedded clay layer was 0.0325, for the homogenous sand profile was 0.0127, and for the homogenous clay profile was 0.0132. Note that SI_{noise} was larger for the embedded sand and clay layers, likely a function of having multiple material types in a single numerical element in the layered zone.

5.2. Sensitivity analysis results

The results from the sensitivity analysis are presented in Figs. 10 through 12. As shown in Fig. 10a, the realizations for the homogenous sand profile generally fall within a relatively narrow band around the baseline, between about 3280 kPa and 5070 kPa, with the exception of the realization associated with the upper bound $H = 75$, which produces a much larger $\bar{q}_c$ of 8542 kPa. Fig. 11a and 12a indicate that, by far, the parameter dominating the sensitivity in the homogenous sand simulations is H. Other fairly significant contributions are from D_R, φ_{cont}, χ, and the radial boundary condition. SIs associated with σ'_{ho}, λ, φ_{cs}, and CC radius are less significant. Uncertainty in N, G_{ref} and ν have essentially no impact on $\bar{q}_c$, with SIs falling just at or below SI_{noise} (dashed line in Fig. 12a).

Two trends observed in Fig. 11a highlight the differences in soil behavior resulting from a rigid boundary condition (used as the baseline

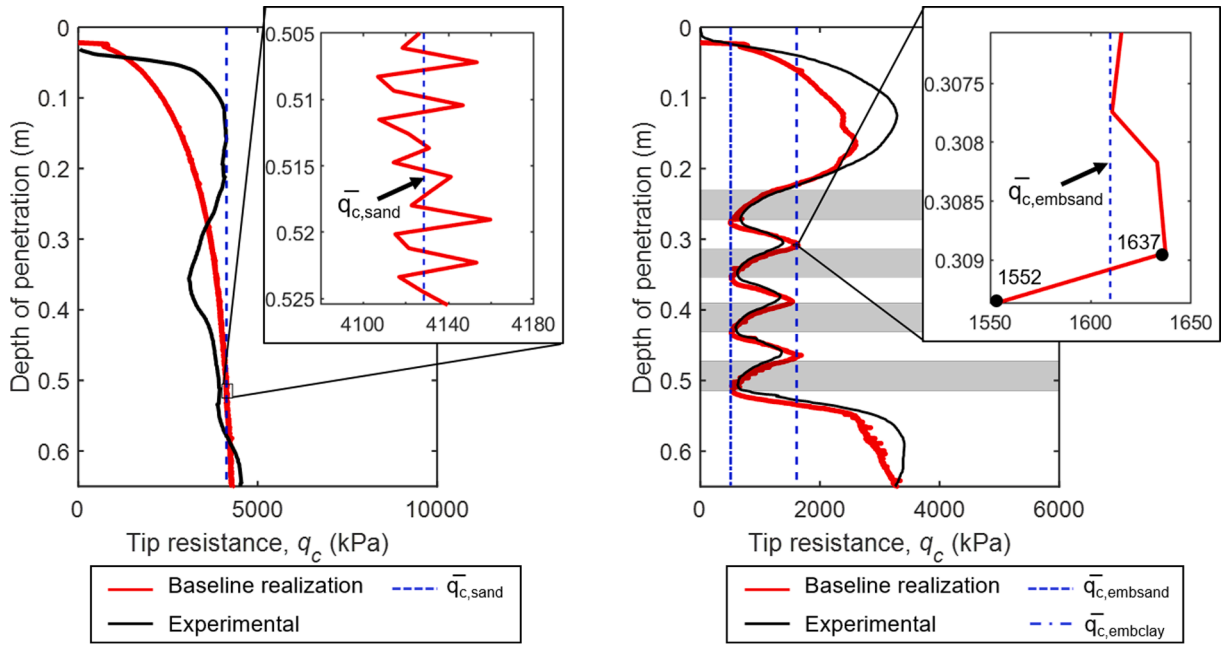

Fig. 9. Baseline tip resistance (q_c) realizations from MPM simulations compared with experimental data, and determination of average tip resistance ($\bar{q}_c$) for (a) homogenous sand profile and (b) layered sand-clay profile. Insets indicate depth ranges over which $\bar{q}_c$ was computed.

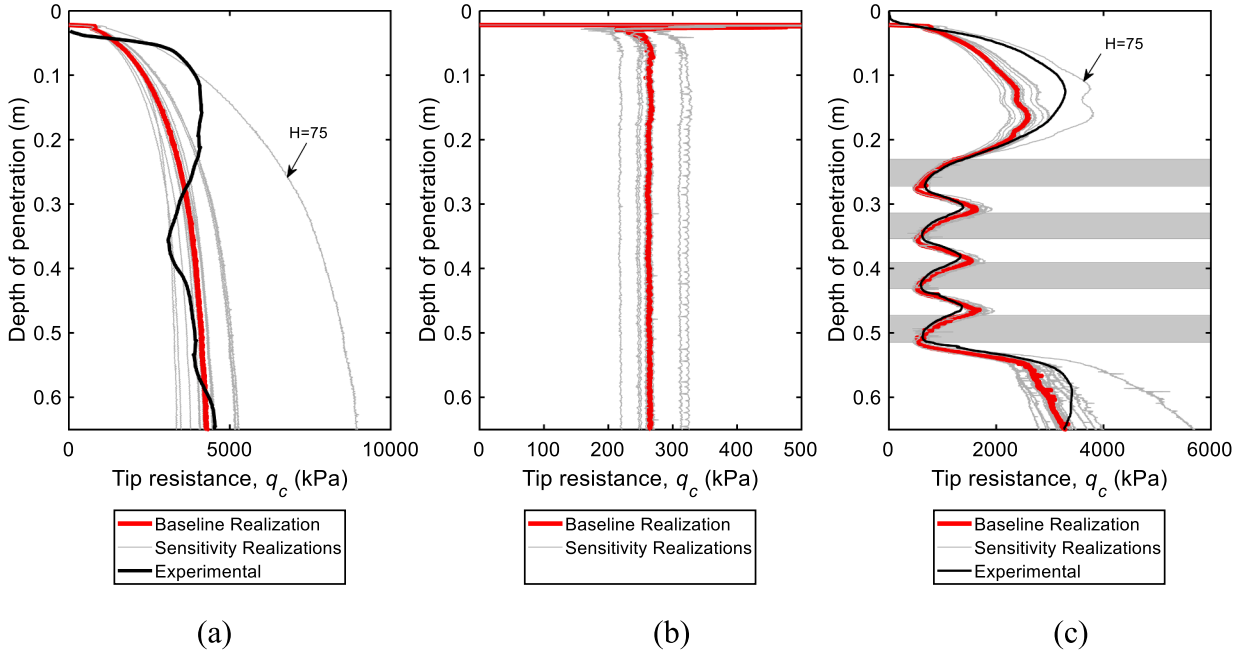

Fig. 10. All realizations from the sensitivity analysis compared to the baseline realization and experimental data for three soil profiles: (a) homogenous sand, (b) homogenous clay, and (c) layered sand-clay, where shaded zones represent clay layers.

condition in these analyses) and a flexible boundary condition (which tends to dominate in literature): (1) Increasing σ'_{ho} resulted in minimal change (very slight decrease) in $\bar{q}_c$. These results are contrary to literature for chambers with flexible boundary conditions that report a clear increase of $\bar{q}_c$ with σ'_{ho} (e.g., Fioravante et al., 1991). The MPM simulation was repeated with a flexible boundary and the results (presented and elaborated on in Section 6.2) are consistent with literature; (2) Decreasing the CC radius resulted in a slight increase in $\bar{q}_c$, consistent with observations from Pournaghiazar et al. (2012; 2013) for rigid boundary conditions. Supplemental simulations were performed with a flexible boundary condition and showed the opposite trend (i.e., decreasing CC radius resulted in a decreased $\bar{q}_c$), consistent with observations from literature for a flexible boundary condition (e.g., Ghionna and Jamiolkowski, 1991).

As shown in Fig. 10b, the realizations for the homogeneous clay profile produced $\bar{q}_c$ values ranging from 230 kPa to 342 kPa compared to the baseline $\bar{q}_c = 264$ kPa. Fig. 11b and 12b show that uncertainty in G and s_u – constitutive parameters of the clay – dominate the uncertainty

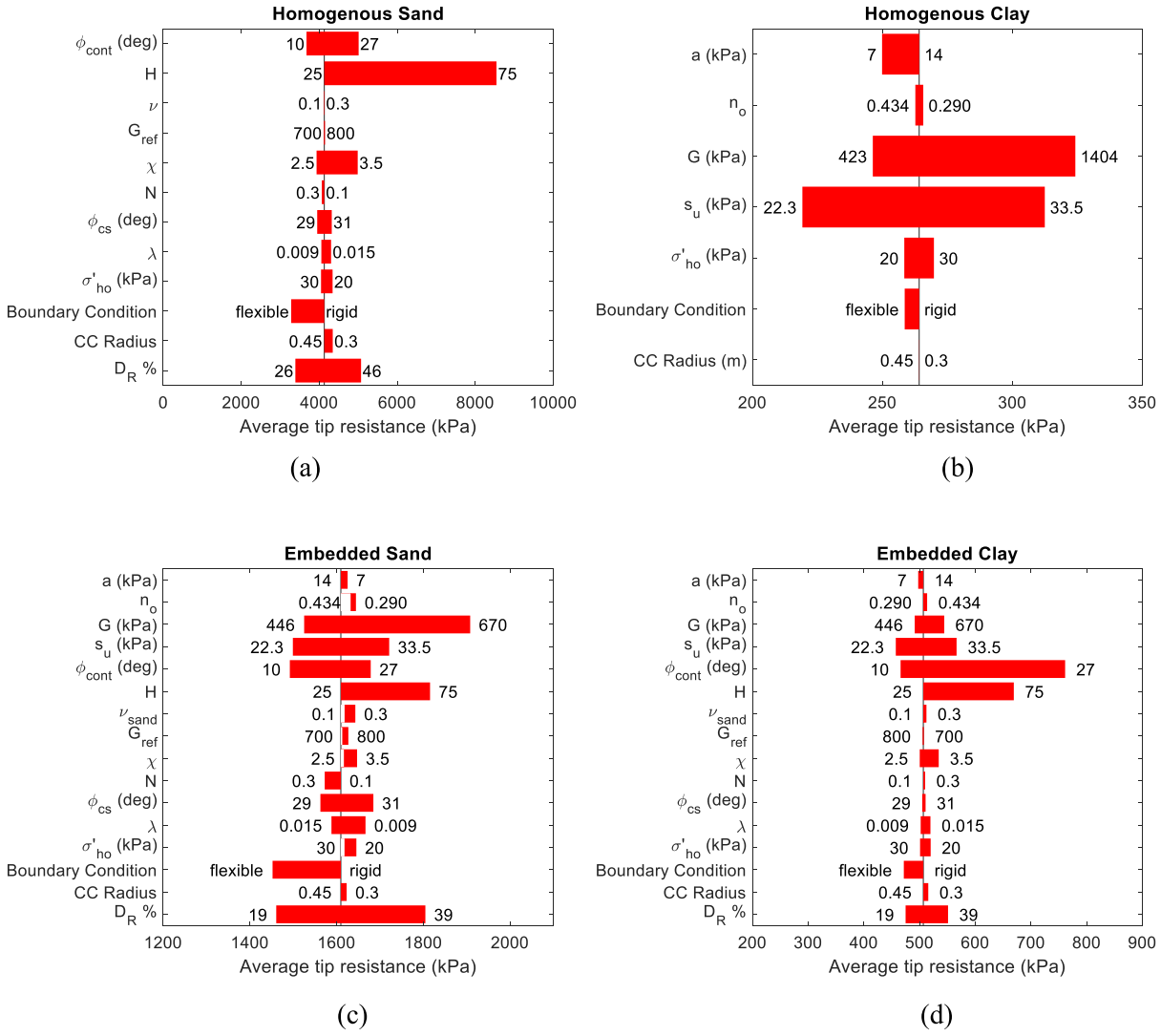

Fig. 11. Range of average tip resistance ($\bar{q}_c$) values obtained by varying a single parameter from the upper to lower bound value indicated on either side of the bar (a) Homogeneous sand profile, (b) Homogeneous clay profile, (c) Embedded sand layer in layered profile, and (d) Embedded clay layer in layered profile.

in $\bar{q}_c$. Contributions from a and σ'_{ho} are less significant, but above SI_{noise}. SI associated with the radial boundary condition, CC radius and n_o fall just at or below SI_{noise}. Notably, increasing σ'_{ho} resulted in a slight increase in $\bar{q}_c$, contrary to what was observed for the homogenous sand profile. In the homogenous clay profile with the Tresca constitutive model, the increased σ'_{ho} slightly increases p', and p' remains elevated for the duration of penetration resulting in a slightly increased $\bar{q}_c$.

The realizations from the layered profile are shown in Fig. 10c. For the embedded sand, uncertainty in G (of the clay) and D_R (of the sand) resulted in the most uncertainty in q_c (see Fig. 11c and 12c). Contributions from H, φ_{cont}, and radial boundary condition fall above the noise level; all other parameters fall below. In Fig. 12c, a few of the bars (n_o, ν of sand, G_{ref}, χ, and σ'_{h_o}) do not touch the baseline value, meaning the realization using the lower bound parameter resulted in a larger $\bar{q}_c$ than the baseline realization. This is simply a reflection of the significance of the noise level. For the embedded clay layer, SI was largest for φ_{cont} and H. s_u, G (of the clay), and D_R (of the sand) produced the next largest SIs, followed by χ and the boundary condition. All other parameters produced SIs at or below the level of noise.

6. Discussion

6.1. Sensitivity analysis discussion

The sensitivity analysis results showed that $\bar{q}_c$ of the embedded layers in the layered profile were less sensitive to uncertainties in input parameters than $\bar{q}_c$ of the homogenous profiles. This is likely because q_c is unable to fully develop in the embedded layers, so while changes in input parameters significantly affect the fully-developed q_c in the homogenous profiles, they have less of an impact on the undeveloped q_c in the layered profile. Furthermore, considering only the layered profile, the $\bar{q}_c$ of the embedded sand layers was less sensitive to uncertainties in input parameters than the $\bar{q}_c$ of the embedded clay layers. Similar to the previous explanation, this is likely due to the fact that q_c in the embedded clay layers is much closer to the fully-developed q_c of the clay than q_c in the embedded sand layers is to the fully-developed q_c of the sand. The impact of changes in input parameters will be reflected more in the layers where q_c is closer to the fully-developed q_c (i.e., the clay layers). A final observation is that $\bar{q}_c$ in the embedded clay layers was more impacted by uncertainties in the sand input parameters than the clay input parameters. This is expected since the range of outputs resulting from changes in sand input parameters was significantly larger than that from the clay in the homogenous profiles, as demonstrated by

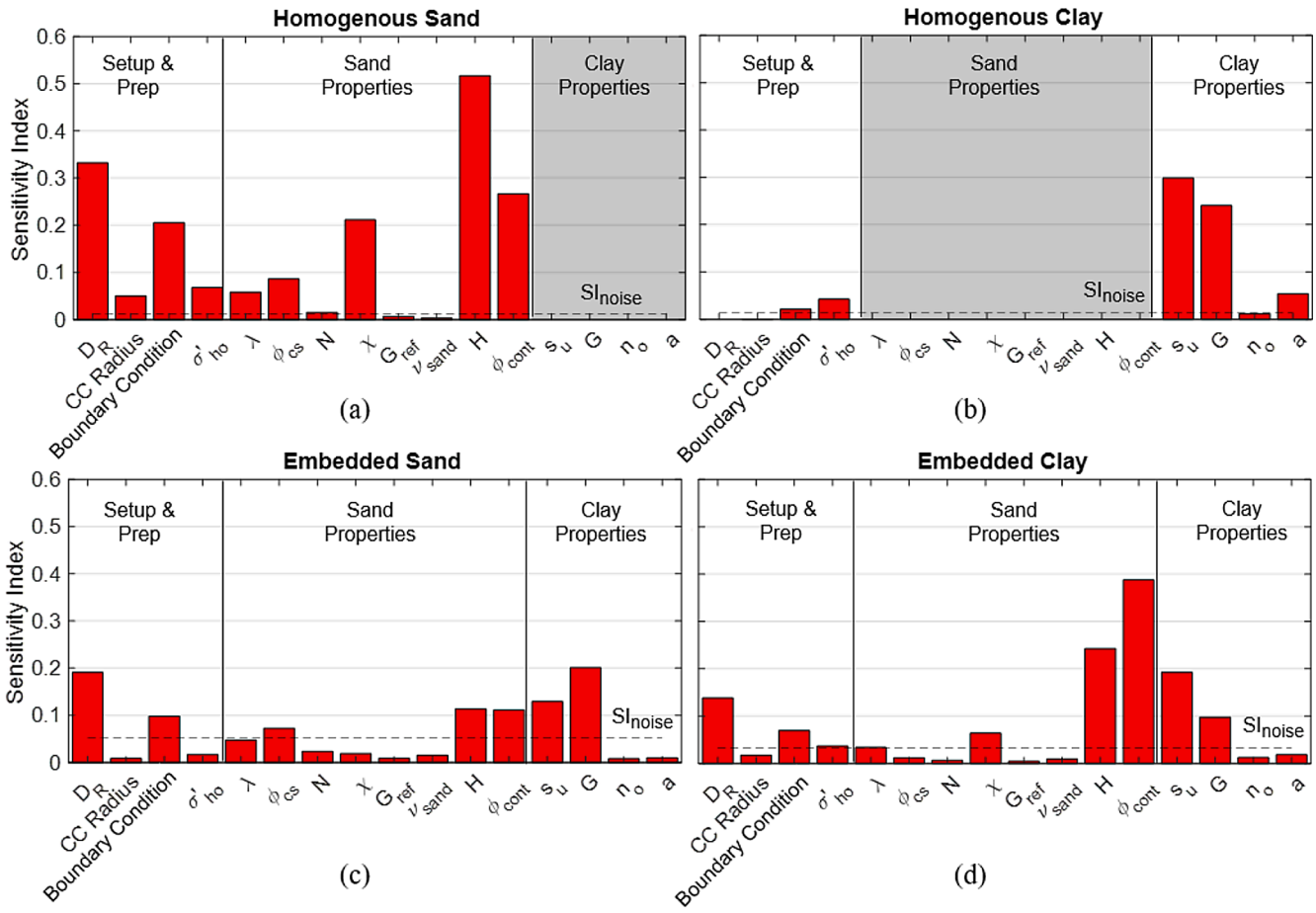

Fig. 12. Comparison of sensitivity index for all soil profiles: (a) Homogeneous sand profile, (b) Homogeneous clay profile, (c) Embedded sand layer in layered profile, and (d) Embedded clay layer in layered profile. Shaded gray zones indicate parameters that are not used in the analysis for that particular profile. Noise levels are indicated with a dashed line at the level of SI_{noise}.

the difference in ranges of q_c demonstrated in Fig. 10a and 10b.

6.2. Impact of radial boundary conditions

In Section 5.2, it was observed that variations in σ'_{ho} had a very minor impact on $\bar{q}_c$ when the rigid radial boundary condition was considered (showed a very slight decrease in $\bar{q}_c$ with increased σ'_{ho}), but literature on flexible boundary conditions indicates that significant increases in $\bar{q}_c$ should be observed with increasing σ'_{ho}. To further explore this, four additional MPM simulations were performed. All simulations corresponded to the homogenous sand profile with D_R = 60% and σ'_{vo} = 100 kPa shown in Fig. 3a. Initial horizontal stresses of σ'_{ho} = 50 kPa and 90 kPa were considered with both rigid and flexible boundary conditions. Tip resistance versus depth for each of the four simulations is shown in Fig. 13. With the rigid boundary, both conditions of σ'_{ho} produce similar tip resistance profiles, with tip resistance tending to be slightly smaller for the σ'_{ho} = 90 kPa case. On the other hand, for the flexible boundary condition, a significant increase in tip resistance is observed with an increased σ'_{ho}.

To help explain the trends shown in Fig. 13, stress paths of MPs located near the penetrating cone for each of the four simulations (σ'_{ho} = 50 kPa and σ'_{ho} = 90 kPa with rigid and flexible boundary conditions) are presented in Fig. 14. Stresses were tracked at three MPs located at distances one, two, and three times the radius of the cone (r_{cone}) away from the axis of symmetry and about 0.5 m deep in the soil profile. For the rigid boundary condition (Fig. 14a), despite the differences in the initial p', the stress paths for the two cases (σ'_{ho} = 50 kPa and σ'_{ho} = 90 kPa) are nearly identical. This is consistent with the observation that

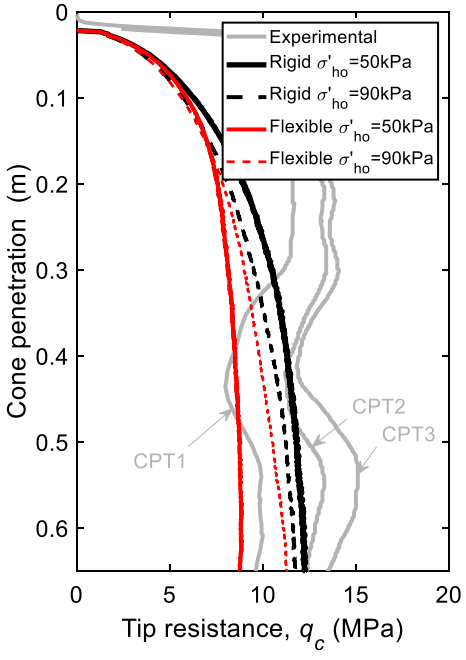

Fig. 13. Comparison of q_c using varying boundary conditions and initial stress states in a homogenous sand profile.

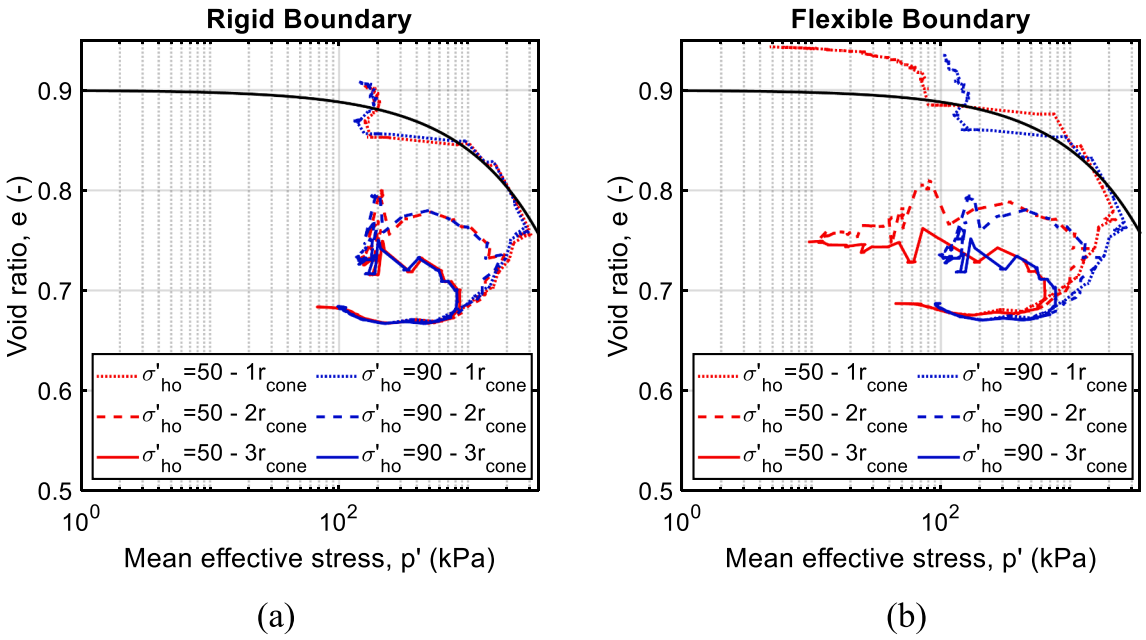

Fig. 14. Stress paths at points located at 1, 2, and 3 times the radius of the cone away from the axis of symmetry for $\sigma'_{ho} = 50$ kPa and $\sigma'_{ho} = 90$ kPa. (a) Stress paths associated with rigid radial boundary condition; (b) Stress paths associated with flexible radial boundary condition.

changes in σ'_{ho} have a very minor effect on $\bar{q}_c$. The fact that $\bar{q}_c$ is slightly smaller for the larger $\sigma'_{ho} = 90$ kPa is also consistent with the fact that p' is slightly smaller throughout the $\sigma'_{ho} = 90$ kPa stress path compared to the $\sigma'_{ho} = 50$ kPa stress path. On the contrary, the stress paths shown in Fig. 14b for the flexible boundary condition are quite different, with p' values generally larger for the $\sigma'_{ho} = 90$ kPa condition. This is consistent with the trends observed in Fig. 13. The impact of the boundary condition on how $\bar{q}_c$ changes with σ'_{ho} is discussed in further detail in the supplemental materials.

6.3. Accounting for multiple CPTs performed in a single profile

Construction of soil profiles for CC tests can be labor intensive and expensive. Therefore, it is advantageous to perform more than one CPT per profile to optimize the amount of data obtained. However, this practice may increase uncertainty in the results and make certain numerical modeling parameters difficult to define. In the De Lange (2018) experimental tests, three CPTs were typically performed in each soil profile in a triangular pattern, 0.26 m apart from each other and 0.3 m from the wall of the CC. After being advanced, the penetrometers were left in place to avoid potential disturbance from removal. When attempting to replicate these experimental tests numerically, the first and perhaps most obvious issue is how to define the CC radius in the 2D axisymmetric simulations. To address this, both the true CC radius (0.45 m) and the shortest distance from the penetrometer to the CC wall (0.3 m) were considered in the sensitivity analyses presented. It is shown in Section 5.2 that variation of the CC radius from 0.45 m to 0.3 m only had a significant impact for the homogenous sand profile. Even for that profile, compared to several other input parameters with SI > 0.2, the impact of changing radius was still relatively small with an SI ≈ 0.05. It is therefore concluded that the baseline condition with a 0.45-m radius is a good approximation of the laboratory conditions. The second issue with performing multiple CPTs in one profile is whether each CPT has an impact on a subsequent CPT. This seems to be the case in these experiments. As previously shown in Fig. 3a, $\bar{q}_c$ increased about 26% between the first and second CPTs. This is happening for two primary reasons: (1) the stress state in the CC is significantly altered with each CPT due to the rigid radial boundary condition, and therefore initial stress conditions are not the same for subsequent CPTs, and (2) local densification occurs adjacent to the cone during penetration and extends into the zone of influence of the subsequent CPTs.

6.3.1. Examining changes in stress state

To investigate the changing stress state in the CC, a MPM simulation was performed to replicate the experimental results from the homogenous sand profile shown in Fig. 3a ($D_R = 60\%$, $\sigma'_{vo} = 100$ kPa, $\sigma'_{ho} = 50$ kPa). Stresses were tracked along the rigid radial boundary at three selected MPs over the course of one CPT, as shown in Fig. 15. Note that stresses computed at the boundary suffer from inaccuracies due to large element sizes, and in particular, stresses computed near the surcharge-soil interface are affected by the non-zero modulus of the surcharge soil. However, important trends are still captured in these plots. With increasing penetration, both σ'_v and σ'_h increase from σ'_{vo} and σ'_{ho} at all depths along the radial boundary. Vertical stresses increase up to about 20%, and horizontal stresses increase up to about 240%, resulting in σ'_h/σ'_v much closer to 1.0 than the initial $\sigma'_{ho}/\sigma'_{vo}$ of 0.5. Consequently, the next CPT in this profile will not experience the same initial stress conditions as the previous one, and we should not expect $\bar{q}_c$ to be the same.

While increasing σ'_{ho} does not tend to increase $\bar{q}_c$ for the rigid boundary condition as discussed in Section 6.2, a 20% increase in σ'_{vo} to 120 kPa (and accompanied increase in σ'_{ho} to 60 kPa to maintain the initial $K_0 = 0.5$ condition imposed in the lab) does produce a $\sim$ 15% increase in $\bar{q}_c$, as shown in Fig. 16. This is less than the $\sim$ 26% increase observed in the lab CC results between the first and second CPTs. Thus, while the change in the initial stress state does impact the results of subsequent CPTs in the CC, it is probably not the only contributor to the increased $\bar{q}_c$.

6.3.2. Local densification during penetration

The second contributor to the increase in $\bar{q}_c$ with subsequent CPTs is local densification during penetration. We observed that by the end of penetration, e was altered within a radius of about 24 cm around the penetrometer. Immediately adjacent to the penetrometer, the soil dilated, but the soil in the rest of this zone of influence contracted. Since the CPTs were performed in this profile at locations 26 cm away from each other, it is reasonable to conclude that the zones of influence would overlap. An example of how this could influence the results was determined by selecting a representative e in the zone of influence at the end

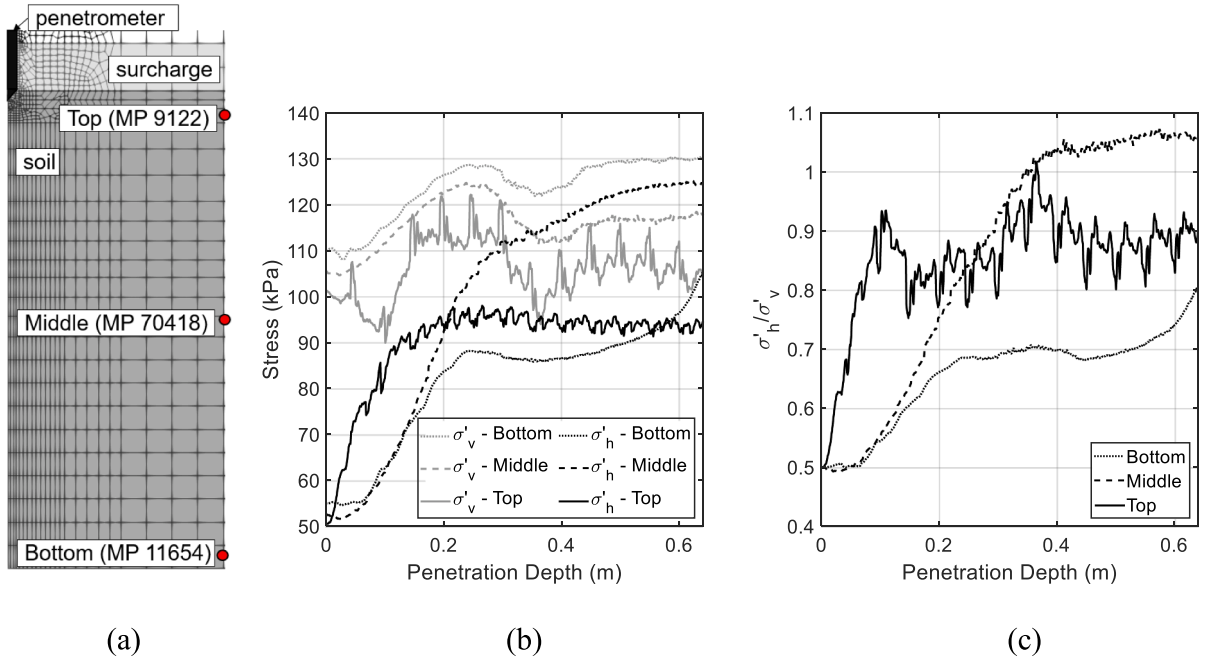

Fig. 15. (a) Position of three material points (9122, 70418, and 11654) along the rigid boundary (fixed in x-direction) in a homogenous sand profile whose stress history is shown in (b) and (c); (b) Evolution of effective vertical and horizontal stresses, σ'_v and σ'_h, along the rigid boundary during CPT penetration; (c) Evolution of σ'_h/σ'_v along the rigid boundary during CPT penetration.

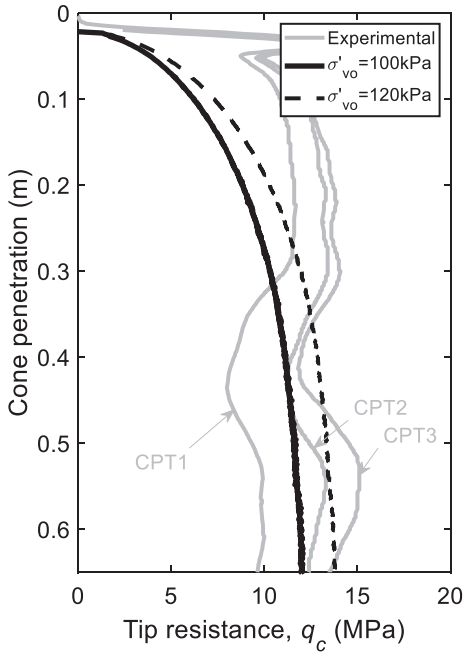

Fig. 16. Impact of increasing σ'_{vo} on q_c when using rigid radial boundary conditions.

of penetration and performing a simulation with a D_R associated with that new e value (and all other conditions held constant). For example, for the simulation with results shown in Fig. 16 as a solid line, the minimum e at the end of penetration was equal to 0.669, corresponding to a $D_R = 65\%$ (compared to the original $D_R = 60\%$). Note that experimental post-test (i.e., after all three CPTs were performed) local density measurements in this profile indicated a D_R of about 70%, making a 5% increase in D_R after one CPT very reasonable. A second CPT simulation performed with an initial $D_R = 65\%$ resulted in a ~ 10% increase in $\bar{q}_c$.

Combining this ~ 10% increase in $\bar{q}_c$ from increased density with the ~ 15% increase from the modified stress conditions, the 26% increase in $\bar{q}_c$ observed in the lab is accounted for quite well.

6.4. *Reducing uncertainty in experimental CC tests and their numerical counterparts*

Based on the findings in this study, the following recommendations are provided to reduce uncertainty in both the experimental and numerical aspects of CC testing:

Experimental setup/methods and numerical model geometry/boundary conditions:

- Perform CPTs only at the center of the CC to ensure axisymmetric conditions and to have a well-defined CC radius. Alternatively, quantify the impact of performing a CPT at the center versus an off-center (i.e., closer to the boundary) location by performing a test where multiple CPTs are performed in the same profile without changing σ'_{vo}.
- Understand the limitations of the CC in applying the desired boundary conditions.
- Perform only one CPT per soil profile to avoid changing initial stress conditions and local densities prior to subsequent CPTs. Alternatively, since preparing calibration chamber samples is extremely labor intensive, show that subsequent CPTs are not impacted by previous ones or quantify the impacts of performing multiple CPTs in one profile experimentally and numerically. Numerical simulations seeking to validate results may choose to use the first experimental CPT performed in each laboratory calibration chamber soil profile to avoid these concerns.
- Use a calibration chamber with radius large enough to allow multiple CPTs to be performed without impacting stress or density conditions for subsequent CPTs.

Soil profile preparation and numerical model initial conditions:

- Minimize and quantify variation in as-prepared D_R of the sand. For example, take local density measurements after testing and compare results from CPTs performed in different locations in the CC. The latter is useful in identifying, for example, the presence of a looser horizontal layer in an otherwise homogenous sample (indicated by multiple CPT soundings with decreased q_c within the same depth range), even with the acknowledgement that local D_R may have been impacted by performing CPTs in multiple locations. Ideally, for this assessment, the chamber would be large enough to avoid local D_R changes impacting consecutive CPTs.
- Quantify changes in D_R over the course of CC testing. For example, the increase in D_R caused by increased loading may be quantified experimentally by measuring outflowing water during sample pressurization and comparing post-test density measurements with pre-test density measurements. Experimentally quantifying local increases in D_R caused by cone penetration is a more difficult task but may be done numerically as demonstrated in this article.
- Consider using multiple D_R values in numerical simulations to model even a "homogenous" sand profile (i.e., break the sand profile into layers) if local variations in D_R are significant.
- Measure depth to layer boundaries from a common reference point before and after each CPT, as close to the CPT as possible. Link penetrometer position to true depths in the profile (i.e., ensure the zero depth of the CPT sounding is equal to the zero depth of the soil profile) at the time of the experiment.

Soil properties and constitutive modeling of soil properties:

- Accompany experimental CC tests with a thorough laboratory strength testing program. Ideally, the program should be specifically designed to obtain the parameters needed for constitutive models of interest, so that corresponding numerical models of the CC tests do not need to rely on external literature to estimate constitutive parameters.
- Minimize the contribution of uncertainty from model parameters with no physical significance (e.g., H) by performing additional laboratory tests or extending calibration efforts. Further work is needed to quantify how H varies as a function of both ψ_o and p'_o, rather than just ψ_o.
- Quantify contact properties between the cone and soil through laboratory interface testing. Contact properties are frequently assumed, but they are shown in this study to have a significant impact on the results.

7. Conclusions

This study addressed the complexities of numerical modeling (e.g., using MPM) of CPTs performed in CCs in homogenous and interlayered soil profiles. It was shown that significant experimental and numerical uncertainties exist in CC tests and can be explored numerically. In this study, uncertainty associated with soil properties and profile preparation, rather than uncertainties associated with the experimental setup (e.g., radial boundary condition, initial stresses, and CC radius), tended to have the most impact on q_c. The sensitivity analysis indicated that the parameters that most significantly impact q_c in the homogenous sand and clay profiles are not necessarily the same ones that most significantly impact q_c in the layered soil profile, and in general, the layered soil profile was less sensitive to uncertainties in input parameters than the homogenous soil profiles. Experimental results show that performing multiple CPTs in a single soil profile results in an increased average q_c; this observation was explained numerically and attributed to changing stress states and local densities caused by penetration. Finally, recommendations for improving future experimental and numerical CC studies (especially in layered profiles) were provided, suggesting additional data collection is needed to better quantify uncertainty.

CRediT authorship contribution statement

Kaleigh M. Yost: Conceptualization, Methodology, Investigation, Formal analysis, Validation, Writing – original draft, Writing – review & editing. **Mario Martinelli:** Conceptualization, Methodology, Investigation, Software, Writing – review & editing. **Alba Yerro:** Methodology, Investigation, Writing – review & editing. **Russell A. Green:** Methodology, Investigation, Writing – review & editing. **Dirk A. de Lange:** Investigation, Resources, Writing – review & editing.

Declaration of Competing Interest

The authors declare that they have no known competing financial interests or personal relationships that could have appeared to influence the work reported in this paper.

Data availability

Data will be made available on request.

Acknowledgements

This research was partially funded by National Science Foundation (NSF) Grant Nos. CMMI-1825189 and CMMI-1937984 and the Institute for International Education Graduate International Research Experience (IIE-GIRE) program supported by NSF under Grant No. 1829436. This support is gratefully acknowledged. Additionally, we thank Deltares for serving as the host institution for the duration of the IIE-GIRE program, for the use of a version of Anura3D software developed in-house by them, and the discussions regarding the experimental tests used in this investigation. We also thank Dr. Adrian Rodriguez-Marek for providing review comments. However, any opinions, findings, conclusions, or recommendations expressed in this material are those of the authors and do not necessarily reflect the views of NSF or others acknowledged.

Appendix A. Supplementary data

Supplementary data to this article can be found online at https://doi.org/10.1016/j.compgeo.2023.105378.

References

Al-Kafaji, I.K.J., 2013. Formulation of a Dynamic Material Point Method (MPM) for Geomechanical Problems. Univ. of Stuttgart, Germany. PhD dissertation.

Bardenhagen, S.G., Guilkey, J.E., Roessig, K.M., Brackbill, J.U., Witzel, W.M., Foster, J. C., 2001. An improved contact algorithm for the material point method and application to stress propagation in granular material. CMES – Comput. Model. Eng. Sci. 2 (4), 509–522. https://doi.org/10.3970/cmes.2001.002.509.

Bardenhagen, S.G., Kober, E.M., 2004. The generalized interpolation material point method. CMES – Comput. Model. Eng. Sci. 5 (6), 477–495. https://doi.org/10.3970/cmes.2004.005.477.

Beuth, L., 2012. Formulation and application of a quasi-static material point method. Univ. of Stuttgart, Germany. PhD dissertation.

Beuth, L., Vermeer, P.A., 2013. Large deformation analysis of cone penetration testing in undrained clay. In: Hicks et al. (Eds), Installation Effects in Geotechnical Engineering. Taylor & Francis Group, London. ISBN 978-1-138-00041-4.

Bisht, V., Salgado, R., Prezzi, M., 2021. Analysis of Cone Penetration Using the Material Point Method. In: Barla et al. (Eds), IACMAG 2021, LNCE 125. Springer, pp. 765–77. https://doi.org/10.1007/978-3-030-64514-4_81.

Bisht, V., Salgado, R., Prezzi, M., 2021a. Material Point Method for Cone Penetration in Clays. J. of Geotech. Geoenviron. Eng. 147 (12), 1–16. https://doi.org/10.1061/(asce)gt.1943-5606.0002687.

Bødker, L., 1996. Gmax for sand by bender elements at anisotropic stress states. In: Proc. of the XII Nordiska Geotechnical Conference: NGM-96, 26-28 June 1996, Reykjavik, Iceland, pp 93–98.

Boulanger, R.W., DeJong, J.T., 2018. Inverse filtering procedure to correct cone penetration data for thin-layer and transition effects. In: Hicks, Pisano, & Peuchen (Eds.), Proc. of Cone Penetration Testing 2018 (CPT'18), June 21-22, 2018, Delft, the Netherlands. CRC Press, pp. 25–44. https://doi.org/10.1201/9780429505980.

Butlanska, J., Arroyo, M., Gens, A., 2010. Size effects on a Virtual Calibration Chamber. In: Numerical Methods in Geotechnical Engineering. CRC Press, pp. 225–230. https://doi.org/10.1201/b10551-43.

Ceccato, F., Beuth, L., Simonini, P., 2016a. Analysis of Piezocone Penetration under Different Drainage Conditions with the Two-Phase Material Point Method. J. Geotech. Geoenviron. Eng. 142 (12), 04016066. https://doi.org/10.1061/(asce)gt.1943-5606.0001550.

Ceccato, F., Beuth, L., Vermeer, P.A., Simonini, P., 2016b. Two-phase Material Point Method applied to the study of cone penetration. Comput. Geotech. 80, 440–452. https://doi.org/10.1016/j.compgeo.2016.03.003.

Ceccato, F., Beuth, L., Simonini, P., 2015. Study of the effect of drainage conditions on cone penetration with the Material Point Method. In: Proc. of the XV Pan-American Conference on Soil Mechanics and Geotechnical Engineering, 15-19 November 2015, Buenos Aires, Argentina.

Ceccato, F., Simonini, P., 2017. Numerical study of partially drained penetration and pore pressure dissipation in piezocone test. Acta Geotechnica 12, 195–209.

Chapman, G.A., 1974. A calibration chamber for field test equipment. In: Proc. of the European Symposium on Penetration Testing, ESOPT, 5-7 June 1974, Stockholm, Sweden.

Cooper, J., Martin, E.R., Yost, K.M., Yerro, A., Green, R.A., 2022. Robust identification and characterization of thin soil layers in cone penetration data by piecewise layer optimization. Comput. Geotech. 141, 104404. https://doi.org/10.1016/j.compgeo.2021.104404.

De Lange, D.A., 2018. CPT in Thinly Layered Soils. In: Van Elk, J., Doornhof, D., (Eds.), NAM.

Durgunoglu, H.T., Mitchell, J.K., 1973. Static Penetration Resistance of Soils Technical Report. Berkeley, CA: Space Sciences Laboratory.

Eid, W.K., 1987. Scaling effect in cone penetration testing in sand. PhD dissertation. Virginia Tech, USA.

Fioravante, V., Jamiolkowski, M., Tanizawa, F., Tatsuoka, F., 1991. Results of CPT's in Toyura quartz sand. In: A.-B. Huang (Ed.), Proc. 1st Int. Symposium on Calibration Chamber Testing/ISOCCT1, 28-29 June 1991, Potsdam, New York. Elsevier, pp. 135–146.

Galavi, V., Tehrani, F.S., Martinelli, M., Elkadi, A., Luger, D., 2018. Axisymmetric formulation of the material point method for geotechnical engineering applications. In: Cardoso et al. (Eds.), Proc. of 9th Conf. on Numerical Methods in Geotechnical Engineering. Taylor and Francis, London, pp. 427–434.

Ghasemi, P., Calvello, M., Martinelli, M., Galavi, V., Cuomo, S., 2018. MPM simulation of CPT and model calibration by inverse analysis. In: Hicks, Pisano, & Peuchen (Eds.), Proc. of Cone Penetration Testing 2018 (CPT'18), June 21-22, 2018, Delft, the Netherlands. CRC Press, pp. 295–301. https://doi.org/10.1201/9780429505980.

Ghionna, V.N., Jamiolkowski, M., 1991. A critical appraisal of calibration chamber testing of sands. In: A.-B. Huang (Ed.), Proc. of the 1st Int. Symposium on Calibration Chamber Testing/ISOCCT1, 28-29 June 1991, Potsdam, New York. Elsevier, pp. 13–40.

Hoffman, F.O., Gardner, R.H., 1983. Evaluation of Uncertainties in Radiological Assessment Models. In: Radiological Assessments: a Textbook on Environmental Dose Assessment, Till, J.E., and Meyer, H.R., eds. https://doi.org/10.2172/5407895.

Holden, J.C., 1991. History of the first six CRB calibration chambers. In: A.-B. Huang (Ed.), Proc. 1st Int. Symposium on Calibration Chamber Testing/ISOCCT1, 28-29 June 1991, Potsdam, New York. Elsevier, pp. 1–11.

Huang, A.-B. (Ed.), 1991. Proc. 1st Int. Symposium on Calibration Chamber Testing/ISOCCT1, 28-29 June 1991, Potsdam, New York. Elsevier.

Hughes, T.J.R., 2000. The Finite Element Method: Linear Static and Dynamic Finite Element Analysis. Prentice-Hall, Englewood Cliffs, NJ.

Ibsen, L.B., Bødker, L.B., 1994. Baskarp Sand No. 15: Data Report 9301. Aalborg: Geotechnical Engineering Group. Denmark, pp. 1-78.

Jefferies, M.G., 1993. Nor-Sand: A simple critical state model for sand. Geotechnique 43 (1), 91–103. https://doi.org/10.1680/geot.1993.43.1.91.

Jefferies, M., Been, K., 2015. Soil liquefaction: A critical state framework approach, 2nd ed. CRC Press, London.

Krage, C.P., Broussard, N.S., DeJong, J.T., 2014. Estimating rigidity index (IR) based on CPT measurements. In: 3rd International Symposium on Cone Penetration Testing (CPT'14), Las Vegas, Nevada, 13-14 May 2014. pp. 727–735.

Li, X.S., Wang, Y., 1998. Linear Representation of Steady-State Line for Sand. J. Geotech. Geoenviron. Eng. 124 (12), 1215–1217. https://doi.org/10.1061/(asce)1090-0241(1998)124:12(1215).

Martinelli, M., 2019. The NorSand model: Implementation and validation. Delft, the Netherlands, Deltares Internal Report.

Martinelli, M., Galavi, V., 2021. Investigation of the Material Point Method in the simulation of Cone Penetration Tests in dry sand. Comput. Geotech. 130, 103923. https://doi.org/10.1016/j.compgeo.2020.103923.

Martinelli, M., Galavi, V., 2022. An explicit coupled MPM formulation to simulate penetration problems in soils using quadrilateral elements. Comput. Geotech. 145, 104697. https://doi.org/10.1016/j.compgeo.2022.104697.

Martinelli, M., Pisano, F., 2022. Relating cone penetration resistance to sand state using the material point method. Geotechnique Lett. 12 (2), 131–138. https://doi.org/10.1680/jgele.21.00145.

Mayne, P.W., Kulhawy, F.H., 1991. Calibration chamber database and boundary effects correction for CPT data. In: A.-B. Huang (Ed.), Proc. of the 1st International Symposium on Calibration Chamber Testing/ISOCCT1, 28-29 June 1991, Potsdam, New York. Elsevier. pp. 257–264.

Parkin, A.K., Lunne, T., 1982. Boundary effects in the laboratory calibration of a cone penetrometer for sand. In: Proc. 2nd European Symposium on Penetration Testing (ESOPT II), 24-27 May 1982, Amsterdam, the Netherlands.

Potyondy, J.G., 1961. Skin friction between various soils and construction materials. Geotechnique 11 (4), 339–353. https://doi.org/10.1680/geot.1961.11.4.339.

Pournaghiazar, M., Russell, A.R., Khalili, N., 2012. Linking cone penetration resistance measured in calibration chambers and the field. Geotechnique Lett. 2, 29–35. https://doi.org/10.1680/geolett.11.00040.

Pournaghiazar, M., Russell, A.R., Khalili, N., 2013. Drained cavity expansions in soils of finite radial extent subjected to two boundary conditions. Int. J. Numer. Analyt. Methods Geomech. 37 (4), 331–352. https://doi.org/10.1002/nag.1099.

Salgado, R., Mitchell, J.K., Jamiolkowski, M., 1998. Calibration Chamber Size Effects on Penetration Resistance in Sand. J. Geotech. Geoenviron. Eng. 124 (9), 878–888.

Salgado, R., Prezzi, M., 2007. Computation of Cavity Expansion Pressure and Penetration Resistance in Sands. Int. J. Geomech. 7 (4), 251–265. https://doi.org/10.1061/(asce)1532-3641(2007)7:4(251).

Schnaid, F., Houlsby, G.T., 1991. An assessment of chamber size effects in the calibration of in situ tests in sand. Géotechnique 41 (3), 437–445. https://doi.org/10.1680/geot.1991.41.3.437.

Shuttle, D., Jefferies, M., 2010. NorSand: Description. Calibration, Validation and Applications.

Simo, J.C., Taylor, R.L., Pister, K.S., 1985. Variational and projection methods for the volume constraint in finite deformation elasto-plasticity. Comput. Methods Appl. Mech. Eng. 51 (1–3), 177–208. https://doi.org/10.1016/0045-7825(85)90033-7.

Skrede, H., Hammer, H.B., Nordal, S., L'Heureux, J.-S., 2022. CPTU-detection of thin clay layers in sand: Results from calibration chamber tests. In: Gottardi, T. (Ed.), Cone Penetration Testing 2022. CRC Press, pp. 690–696. https://doi.org/10.1201/9781003308829-101.

Sulsky, D., Chen, Z., Schreyer, H.L., 1994. A particle method for history-dependent materials. Comput. Methods Appl. Mech. Eng. 118 (1–2), 179–196. https://doi.org/10.1016/0045-7825(94)90112-0.

Talmon, A.M., Martinelli, M., Luger, H.J., 2019. Numerical simulation of cutting tests on layered sand and clay. In: Proc. 22nd World Dredging Congress (WODCON 2019), Shanghai, China, 22-26 April 2019, pp. 462–477.

Tehrani, F.S., Galavi, V., 2018. Comparison of cavity expansion and material point method for simulation of cone penetration in sand. In: Hicks, Pisano, & Peuchen (Eds.), Proc. of Cone Penetration Testing 2018 (CPT'18), June 21-22, 2018, Delft, the Netherlands. CRC Press, pp. 611–615. https://doi.org/10.1201/9780429505980.

Yost, K.M., Green, R.A., Upadhyaya, S., Maurer, B.W., Yerro-Colom, A., Martin, E.R., Cooper, J., 2021. Assessment of the efficacies of correction procedures for multiple thin layer effects on Cone Penetration Tests. Soil Dyn. Earthq. Eng. 144, 106677. https://doi.org/10.1016/j.soildyn.2021.106677.

Yost, K.M., Yerro, A., Green, R.A., Martin, E., Cooper, J., 2022. MPM Modeling of Cone Penetrometer Testing for Multiple Thin-Layer Effects in Complex Soil Stratigraphy. J. Geotech. Geoenviron. Eng. 148 (2), 04021189. https://doi.org/10.1061/(ASCE)GT.1943-5606.0002730.